Materials & Design 257 (2025) 114398

Contents lists available at ScienceDirect

Materials & Design

journal homepage: www.elsevier.com/locate/matdes

From coral to control: bio-inspired, 3D-printable metamaterials with tuneable quasi-zero stiffness and multi-functional bio-composites

Shawn Ravanbod [a], Kaveh Rahmani [a], Sarah Karmel [b], Ira Pande [c], Hoda Amel [d], Callum Branfoot [e], Arash M. Shahidi [f], Andrew Alderson [g], Mahdi Bodaghi [a,*]

[a] Department of Engineering, School of Science and Technology, Nottingham Trent University, Nottingham NG11 8NS, UK
[b] Rheon Labs, Broughton St, London SW8 3QJ, UK
[c] Rheumatology Department, Queen's Medical Centre, Nottingham University Hospitals NHS Trust, Nottingham NG7 2UH, UK
[d] The Manufacturing Technology Centre, Ansty Park, Coventry CV7 9JU, UK
[e] Engineering Operations, National Composites Centre, Bristol BS16 7FS, UK
[f] Advanced Textiles Research Group, Nottingham School of Art and Design, Nottingham Trent University, Waverley Building, Waverley Street, Nottingham NG7 4HF, UK
[g] Materials & Engineering Research Institute, Sheffield Hallam University, Sheffield S1 1WB, UK

ARTICLE INFO

Keywords:
Constant-force metamaterials
Quasi-zero stiffness
Energy dissipation
Bio-inspiration
Bio-composites
3D printing

ABSTRACT

This study introduces a new class of quasi-zero stiffness (QZS) mechanical metamaterials featuring bio-inspired, variable-thickness curvilinear architectures and sustainable, 3D-printable reinforced bio-composites. Drawing inspiration from coral geometries, the proposed metamaterials integrate non-uniform curved beams with programmable plateau regions and controllable constant-force levels. A hybrid framework combining visco-hyperelastic finite element modelling (FEM) with multi-objective optimisation enables geometry tailoring for mechanical precision. FEM is established based on the Mooney Rivlin model in conjunction with Prony series. Reinforcement of thermoplastic polyurethane with 1 wt% Chitosan with antibacterial properties produces a 33 % increase in strength, 152 % enhancement in stress impulse, and over 110 % gain in cyclic energy dissipation, along with 32.5 % burning rate reduction, and better moisture retention. Experimental/numerical analyses confirm stable force–displacement responses, durable hysteresis loops, and negligible Mullins effect over repeated loading–unloading-reloading cycles. The optimised metamaterial achieves a 5 mm plateau-region and tuneable constant-force output ranging from 0.5 to 1.15 N. Additionally, a dual-unit configuration yields double the force capacity while preserving QZS characteristics. This multifunctional platform addresses key limitations in force regulation, overload protection, safety, comfort, hygiene, and sustainability. It demonstrates strong potential for integration into healthcare, sports, and mobility sectors, including orthopaedic devices, rehabilitation grips, and protective sports gears.

1. Introduction

Mechanical metamaterials are rationally developed synthetic structures with specific geometrical arrangements that result in exceptional mechanical properties. These properties include enhanced impact and fatigue resistance [1,2], quasi-zero stiffness (QZS) [3], vibration isolation [4], negative stiffness [5], negative Poisson's ratio (auxeticity) [6], improved energy absorption [7], negative compressibility [8], bandgaps [9], and improved load bearing capability [10]. These outstanding characteristics typically emerge from their distinctive macro- and microstructural configurations, rather than the materials themselves. Modern designs of mechanical metamaterials often draw inspiration from biological materials and structures, including honeycombs, animals, and cells, as well as from molecular and crystalline unit cell layouts [11–14]. Among the various types of mechanical metamaterials, QZS metamaterials have garnered significant attention due to their nonlinear constant-force characteristics. These properties make them well suited for applications involving energy dissipation/absorption, vibration damping, and impact attenuation. As a result, they are promising candidates for emerging applications in areas such as soft robotics fingers and joints [15,16], impact reduction and vibration mitigation in aerospace engineering [17,18], and energy absorption and impact attenuation within the sports industry [19]. Linear absorber systems generally deliver acceptable performance; however, they can be relatively

* Corresponding author.
E-mail address: mahdi.bodaghi@ntu.ac.uk (M. Bodaghi).

https://doi.org/10.1016/j.matdes.2025.114398
Received 22 May 2025; Received in revised form 25 June 2025; Accepted 14 July 2025
Available online 15 July 2025

challenging to adjust when there are changes in load or structural features, which limits their adaptability in complex conditions. In contrast, QZS metamaterials, possessing nonlinear mechanical properties, offer a variety of tailored mechanical behaviours by controlling force–displacement curves during loading. By employing different combinations and programming techniques, these meta-structures can achieve multiple desired mechanical responses, presenting significant potential for enhanced vibration attenuation and energy dissipation.

Likewise, designs for QZS mechanical metamaterials can draw inspiration from nature. Researchers have explored how various exoskeletons, limb joints, and soft tissue structures in living organisms exhibit excellent vibration energy isolation and damping properties, demonstrating a typical QZS mechanism [20–22]. The primary bio-inspired isolation mechanisms are categorised into three types based on the dominant forces involved: stiffness adjustment, auxiliary mass, and damping mechanisms [23]. For instance, Hamzehei et al. [24] developed a printed multi-stiffness wavy metamaterial made of Polylactic Acid (PLA) combined with silk fibres called (PLA silk ultra), aiming at energy dissipation, incorporating shape recovery features inspired by the structure of cactus fibres. Zhou et al. [25] created a tuneable stiffness mechanical metamaterial to enhance energy absorption, based on the limb geometry of a cat, which allows it to fall from heights safely. Yan et al. [26] and Sun et al. [27] introduced bio-inspired QZS metamaterials based on the bird's knee and dog's toe joint, respectively, to improve vibration energy attenuation. Yan et al. [28] developed a paw-inspired structure (PIS), mimicking the fat pad's compensatory effect in digitigrade paws, to improve passive vibration isolation. By counteracting the TLS's negative stiffness through the inherent hardening stiffness of the fat pad, the PIS achieves QZS characteristics and attenuates vibrations above 4 Hz. Conventional QZS mechanical isolators [29,30] are typically designed by integrating a negative stiffness element (such as buckled beams [31], and cam mechanism [32]), with a positive stiffness element (like linear springs [33]) in parallel. This results in a complex isolator that may not be sufficiently compact for applications requiring small scale implementations. The operational range (displacement region) of these QZS attenuators is also quite limited.

Recent advancements in the energy dissipation/absorption features of QZS mechanical metamaterials have led scholars to innovate methods aimed at augmenting constant-force characteristics [17,34]. Strategies under exploration include the expansion of the QZS region or the manipulation of reaction force levels. Notably, curvy configurations [35–40] with flexible movements are effective solutions to the aforementioned problem. Given the excellent shape characteristics of curve and arc-shaped meta-structures, they possess a high load-bearing capacity and exceptional mechanical responses. Optimising the geometrical elements can lead to an almost constant output force across a wide displacement range. To name a few, Zhang et al. [41] proposed a curved mechanical metamaterial with multiple programmable QZS regions for vibration energy absorption, where the goemetry elements were tuned by employing a genetic algorithm (GA). Liu et al. [42] designed a multifunctional sandwich-panel QZS mechanical metamaterial, where the experimental and numerical analyses indicated acceptable vibration isolation and energy absorption. Hong et al. [43] created a 3D printed kirigami-inspired wavy QZS metamaterial using carbon fibre reinforcement, where the structural parameters were tuned through deep reinforcement learning integrated with Bayesian optimisation. Liu et al. [44] introduced a 3D-printed wavy QZS metamaterial with optimised structural parameters, capable of generating a constant force around 2 N with an approximately 3 mm QZR region length using photosensitive resin material. Tang et al. [45] developed a curved beam resonator with inclined beams and a lumped mass, demonstrating controllable QZS properties. Numerical and experimental results showed its effectiveness in generating low-frequency band gaps for vibration attenuation.

Despite the necessity for QZS metamaterials to support loads (known as payloads), previous studies have primarily focused on design geometries aimed solely at enhancing the quality of the QZS length. While the QZS characteristics of metamaterials stem from their unique geometries, the material properties also play a critical role in influencing their constant-force levels and energy absorption capacities. Notably, hyper-elastic materials with hysteresis can demonstrate exceptional energy dissipation due to their viscosity and significant hyper-elasticity, allowing them to absorb more energy as they can tolerate substantial displacement [46,47]. From this perspective, another enhancement in developing QZS mechanical metamaterials can involve customising the constant-force (i.e., payload) level and adjusting mechanical properties through a proper material selection. For instance, Bodaghi et al. [48] introduced a 4D-printed QZS metamaterial featuring hyper-elastic properties of soft polymers and elasto-plastic behaviours of shape memory polymers (SMPs). Their study found that these meta-structures effectively dissipate energy and exhibit mechanical hysteresis with non-coincident compressive loading and unloading curves. FlexPro thermoplastic polyurethane (TPU) filaments were used as soft elastomers, while polyurethane-based SMP filaments with a glass transition temperature of 60 °C served as hard materials. Rezaei et al. [49], and Hamzehei et al. [50] developed 3D-printed auxetic QZS metamaterials using TPU materials. Their results showed high energy dissipation levels due to hyper-elasticity. Bodaghi et al. [51] developed a meta-bio-composite with QZS properties through material reinforcement. The bio-composite filaments were made from the combination of polylactic acid (PLA) and bamboo charcoal, printed using a modified dual-feed printer for bio-composite filaments and continuous flax fibres.

Despite growing interest in QZS metamaterials, most studies continue to focus mainly on geometric design, optimising only for plateau length or stiffness tuning, while neglecting critical performance factors under cyclic conditions. However, real-world applications such as wearables and energy-absorbing systems demand materials that can endure repeated loading without degradation in stiffness or force/displacement output. Moreover, the integration of programmable constant-force behaviour with adaptability to diverse operational environments remains largely unresolved. A major shortcoming is the widespread reliance on purely linear elastic or plastic materials, which offer limited damping and deformability. Hyper-elastic materials with inherent hysteresis, however, can significantly enhance energy dissipation, particularly under large deformations. Yet, few studies explore the synergy between geometry and advanced material systems. In parallel, challenges related to manufacturability, 3D printability, wettability, and flame retardancy are seldom addressed. These gaps limit the scalability and functionality of QZS systems, particularly in domains such as healthcare, sports, and rehabilitation, where safety, flame retardancy, hygiene, and durability are paramount.

A novel class of multifunctional, sustainable QZS mechanical metamaterials was conceptualised through bio-inspired variable-thickness curvilinear designs and developed using a hybrid framework integrating finite element modelling (FEM) with evolutionary-based multi-objective optimisation. Drawing inspiration from coral geometries, the metamaterials offer programmable plateau regions and controllable constant-force responses. The time-dependent visco-hyper-elastic behaviour of the bio-composites was captured via a Mooney–Rivlin five-parameter model augmented by Prony series, enabling accurate prediction of hysteresis loops and cyclic energy dissipation. Bio-based TPU was reinforced with 1 % and 3 % Chitosan with antibacterial properties, with 1 % identified as optimal for enhancing stiffness, hysteretic damping, and flame retardancy. The meta-structures were fabricated via 3D printing and evaluated experimentally and numerically, demonstrating stable constant-force output, reproducible hysteresis loops, and suppressed Mullins effect over multiple cycles. These combined structural and material advancements position the proposed metamaterial as a scalable platform for programmable force control, impact mitigation, overload protection, and cyclic energy dissipation in healthcare, rehabilitation, and sports applications.

2. Metamaterial design and methodology

This study advances the development of QZS mechanical metamaterials by exploiting both material and structural properties. Accordingly, this section begins with the reinforcement strategy of the bio-composite material, followed by a comprehensive description of the modelling and design methodology used to develop the proposed QZS metamaterial.

2.1. Bio-composite development

This study introduces a novel multifunctional reinforced bio-composite designed for 3D printing of QZS mechanical metamaterials. Notably, the developed bio-composite showcases a range of mechanical and material properties, including enhanced mechanical strength, effective energy dissipation, improved wettability, antibacterial characteristics, biocompatibility, and flame retardancy. The matrix is composed of Nanovia TPU pellets with shore hardness of 93A and a melting temperature of 185 °C It is a hyper-elastic material known for its excellent flexibility, making it well-suited for applications involving large displacements. However, it is limited by relatively low mechanical strength. To strengthen the matrix and introduce antibacterial properties, Chitosan powder (obtained from Mystic Moments, UK) is incorporated at weight percentages of 1 and 3 wt%. Chitosan is a natural fibre derived from Chitin; a polysaccharide sourced from marine organisms. Its properties closely resemble those of cellulose found in plant fibres. Due to its biodegradable, biocompatible, and moisture-holding attributes, Chitosan is commonly used in cosmetics, including hair, oral, and skincare products. Additionally, its notable antibacterial qualities make the proposed QZS metamaterial particularly suitable for sports and healthcare applications involving direct human contact. Uniform dispersion plays a critical role in determining the appropriate weight percentages of reinforcement materials. Observations during the filament fabrication process revealed that incorporating more than 3 wt% Chitosan powder can lead to increased brittleness and reduced interlayer adhesion in 3D printing.

Fig. 1 depicts the essential steps involved in the production of Chitosan/TPU bio-composite filaments, beginning with the preparation of raw materials (TPU and Chitosan particles), followed by ball milling, extrusion of composite filaments, and the 3D printing process. The manufacturing procedure for the proposed bio-composite filaments is detailed below.

To eliminate moisture before the extrusion process, TPU pellets and Chitosan powder were individually dried in a hot-air drier at 70 °C for 24 h, as illustrated in Fig. 1. Following this, various mixtures were created by incorporating Chitosan particles into TPU at specified weight percentages. The mixtures were then processed in a planetary ball mill to ensure a uniform distribution of Chitosan particles within the TPU pellets, as shown in Fig. 1. Before the extrusion process commenced, the TPU/Chitosan mixtures were again dried in the hot-air drier for 12 h and subsequently extruded using a single extruder device (3devo, Netherlands) to produce filaments with a diameter of 1.75 mm, which is standard for all printed samples. Manufacturing parameters, including temperature and extrusion speed, were fine-tuned to ensure the production of filaments with minimal defects and consistent diameter variations. Table 1 presents the extrusion parameters utilised in the fabrication of the TPU/Chitosan bio-composite filaments.

2.2. Conceptual design and modelling

This section presents two proposed conceptual designs: uniform and non-uniform QZS metamaterials. The first model, referred to as Model I, is a curvilinear QZS metamaterial inspired by the shape of sea corals. The second model, Model II, is a novel non-uniform curvilinear metamaterial developed using RL, featuring enhanced QZS properties. The following discussion provides a detailed explanation of the design method for the basic model (Model I) as well as the optimisation procedure used to create the optimal model (Model II).

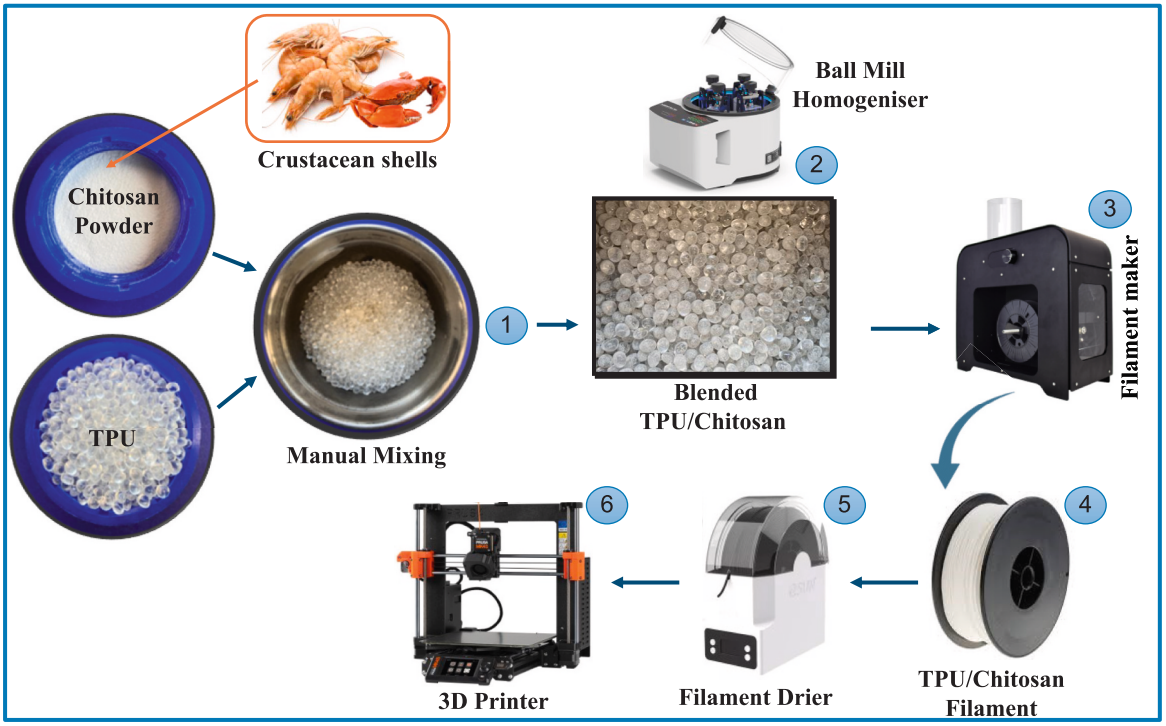

Fig. 1. Schematic representation of the production process for bio-composite materials. Chitosan powder, derived from crustacean shells, is combined with TPU pellets in specified weight percentages. The mixture of TPU and Chitosan undergoes a ball milling process to achieve homogeneity and eliminate agglomeration. Following this, a filament-making process is carried out, after which the resulting TPU/Chitosan filament is dried for 4 h in preparation for the 3D printing process.

Table 1
The extrusion parameters utilised in fabricating the developed bio-composite filaments.

Parameters	Value (TPU)	Value (TPU + 1 %CH)	Value (TPU + 3 %CH)
Extrusion temperature at heat zone 1 (°C)	170	170	180
Extrusion temperature at heat zone 2 (°C)	185	190	200
Extrusion temperature at heat zone 3 (°C)	180	185	192
Extrusion temperature at heat zone 4 (°C)	170	170	180
Die temperature (°C)	180	185	190
Filament diameter (mm)	1.75	1.75	1.75
Extrusion speed (rpm)	3.5	3.5	3.5

2.2.1. *Uniform curved QZS metamaterials*

Drawing inspiration from marine corals, a fundamental meta-structure is designed to replicate the shape-shifting behaviour exhibited by corals in response to ocean waves. This adaptation helps diminish incoming vibrational wave energy and dissipate it (see Fig. 2(I)). The bio-inspiration raised from the multi-curved beams and variable-thickness shape of coral branches, as displayed in Fig. 2(I). The coral branches contribute to the plant's ability to withstand wave energies and maintain their position. Research conducted by geographers has demonstrated that sea corals serve as essential components, functioning as natural breakwaters that protect coastlines from storms and sea waves [52–54]. The exceptional vibration dissipation characteristics and mechanical performance of corals can be attributed to their hierarchical porosity, which spans from the nano to the macro scale. These porous structures effectively absorb and dissipate vibrational energy, with the combination of solid struts and voids functioning as a natural lattice damping system [55]. Marine corals commonly display a gradient in stiffness, consisting of denser outer layers and more porous inner cores. This gradient behaves similarly to engineered metamaterials, where vibration is progressively reflected, refracted, or absorbed, thereby minimising its transmission. Consequently, vibrations are scattered and transformed into heat through internal friction and the effects of micro-inertia. Additionally, some corals demonstrate repeating skeletal patterns that can be modelled as periodic unit cells in mechanical metamaterials. These unit cells can exhibit phononic band gaps (BG) or nearly QZS properties, making them effective for vibration isolation

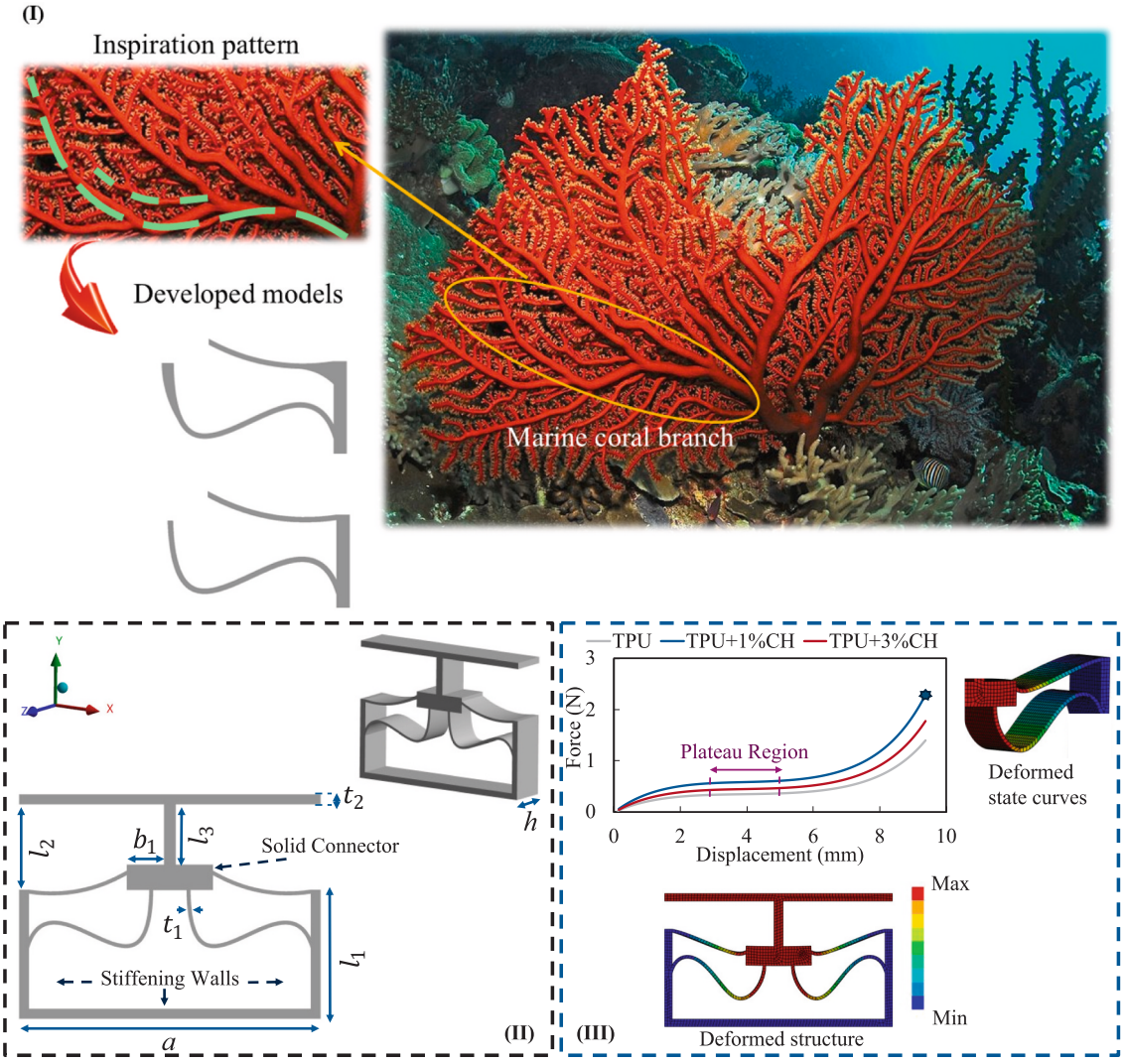

Fig. 2. Design and force–displacement behaviour of the proposed initial model. (I) Modelling the dual-curved QZS metamaterial inspired by the shape of marine coral branches. (II) Illustrates the designed initial QZS meta-structure with determined structural parameters. (III) demonstrates the force–displacement characteristics of the designed initial model, tested using three different materials: TPU, TPU + 1 % Chitosan, and TPU + 3 % Chitosan. The graph indicates that the reinforced bio-composite TPU + 1 % Chitosan has elevated the force levels while maintaining the plateau region. Additionally, the deformation mode of Model I is depicted, highlighting the substantial deformation and snap-through motion of the curved beams that characterise the QZS properties.

within specific frequency bands. Coral branches with irregular and variable sinusoidal (curved) beams and semicircular arches buckle under ocean wave loads, generating both negative and positive stiffness, which collectively results in minimal resistance to small dynamic displacements [52,56]. For instance, Goffredo et al. [57] studied the cyclic force–displacement behaviour of Balanophyllia europaea corals using nanoindentation measurements with a maximum load of 50 mN. The results demonstrated a plateau region between 0 and 30 nm. The hierarchical porosity, variations in stiffness, and the QZS properties observed in certain recurring skeletal patterns, have inspired us to adopt these patterns for the development of QZS metamaterials. The developed QZS meta-composite exhibits similar material and mechanical properties, where the chemical and mechanical interlocking between the TPU matrix and Chitosan particles enhances energy dissipation. The addition of Chitosan introduces interfaces within the TPU matrix, allowing for frictional slippage between TPU particles and the matrix when external loads are applied. This interaction leads to effective mechanical energy dissipation and improved damping properties in the bio-composites. The details of this phenomenon will be discussed comprehensively in the results section. Furthermore, the designed variable-thickness curvature metamaterial exhibits QZS properties, which is able to create a broad programmable plateau region with consistent force and energy dissipation characteristics. By mimicking coral geometries and combining elements that yield controlled negative and positive stiffness contributions, we created biomimetic QZS isolators.

The proposed unit cell comprises two curved beams, each with a uniform thickness and possessing negative-positive stiffness characteristics that generate QZS properties with a wide plateau region. The 3D models in this research were designed using SolidWorks. The structural parameters are outlined in Fig. 2, with the curve thickness emerging as the most influential factor. These curved beams are critical for producing QZS properties, while the solid connector serves to mitigate stresses on the beams during the deformation of the meta-structure. Furthermore, the stiffening walls (supporters) enable the curved beams to undergo substantial deformation, thereby exhibiting QZS characteristics. Parametric analysis was conducted on Model I to determine the sizes of geometry parameters listed in Table 2. The findings from the parametric analysis are presented in section 5.5.

2.2.2. Non-uniform curved QZS metamaterials

This project introduces an innovative bio-inspired mechanical metamaterial featuring non-uniform curvatures (Model II) that exhibits remarkable QZS properties. The material used is the developed sustainable bio-composite. A multi-GA was employed to automatically generate an optimal design using artificial intelligence (AI), starting from the initial model. The objective function aims to maximise the plateau region (d) while simultaneously increasing the reaction force (f). To achieve this, the finite element modelling ANSYS (Version 2024R1, Ansys Inc., CITY, PA, Pennsylvania, USA) software package was integrated with MATLAB (Version R2023b, The MathWorks Inc., MA, USA). This integration allows the algorithm to update control parameters based on feedback and subsequently provide new geometry sizes to the FEM software. The objective functions were calculated, evaluated against stopping criteria, and subjected to constraints (see Fig. 3(I)).

Table 2
Structural parameters used in Model I.

Parameters	Value (mm)
l_1	32
l_2	21.2
l_3	15
t_1	1
t_2	2.5
a	75
h	10

A sensitivity analysis was conducted on the initial design using ANSYS to identify the influential structural parameters affecting the model's QZS characteristics before commencing the optimisation process. The sensitivity analysis revealed that the thickness of the curved segments plays the most significant role in determining the reaction force level and the length of the QZS region. As a result, the controlling parameters were determined through the interpretation of the sensitivity analysis findings, detailed in Table 3. The results of this parametric analysis are presented in the Results and Discussion section. The multi-GA has proposed a non-uniform (i.e., variable-thickness) dual-curved QZS mechanical metamaterial, as illustrated in Fig. 3(I), enhancing the plateau region to approximately 5 mm while shifting the constant force. The meta-structure proposed by the algorithm is novel in the field, as to date, no QZS structures with optimised variable-thickness beams exist. It has been shown that using variable thickness in meta-beams can improve QZS properties. In addition, the specification of the multi-GA process is provided in Table 4 and Fig. 3(II). Five control points were established on the lower layer of the curved beams, determining the thickness of the beams and the shapes of the underlying layers. In contrast, the shape of the upper layers, obtained from parametric analysis, remained unchanged. The ranges for these controlling parameters are listed in Table 3. The multi-GA first received the FEM results from ANSYS, interpreted the data against stopping criteria and constraints explained in the flowchart, and attempted to create the next population with new parameter sizes. These new sizes were then translated to FEM simulations, where numerical analyses were conducted with the updated geometry. The results were sent back to MATLAB for evaluation by the multi-GA, and this iterative process continues until the objective functions met the stopping criteria.

2.3. 3D printing and experimental testing

This section elaborates on the manufacturing process and the experimental testing setup. It provides a detailed account of the fabrication process for dog-bone samples and meta-structures, followed by a description of the procedures for conducted experiments, including microstructural testing, mechanical testing, wettability assessment, and evaluations of flame retardancy.

2.4. Manufacturing process

To produce the bio-composites (TPU, TPU + 1 %CH, and TPU + 3 % CH), 3D printing using Fused Filament Fabrication (FFF) was utilised. Dog-bone samples and proposed metamaterials were fabricated using a PRUSA MK4S printer. The 3D printing parameters employed during fabrication are detailed in Table 5.

2.5. Microstructural evaluation

Scanning electron microscopy (SEM) was employed to examine microstructural details of the developed composites, including aspects such as bonding, fracture surfaces, printing quality, and uniformity levels. A JSM-7100F LV FEG machine was employed for this purpose. Prior to imaging, the samples were coated with a 5 *nm* layer of gold (density: 19.32 $\frac{g}{m^3}$), to enhance image clarity.

2.6. Mechanical test

The mechanical properties of the reinforced bio-composites were assessed through tensile tests conducted using a Shimadzu AG-X Plus machine (with 1kN load capacity). For this evaluation, dog-bone samples of ASTM D-638 Type I were prepared for the bio-composites TPU, TPU + 1 %CH, and TPU + 3 %CH, as illustrated in Fig. 4(I).To mitigate the impact of manufacturing and printing variations on the mechanical properties, five dog-bone samples were fabricated and tested for each

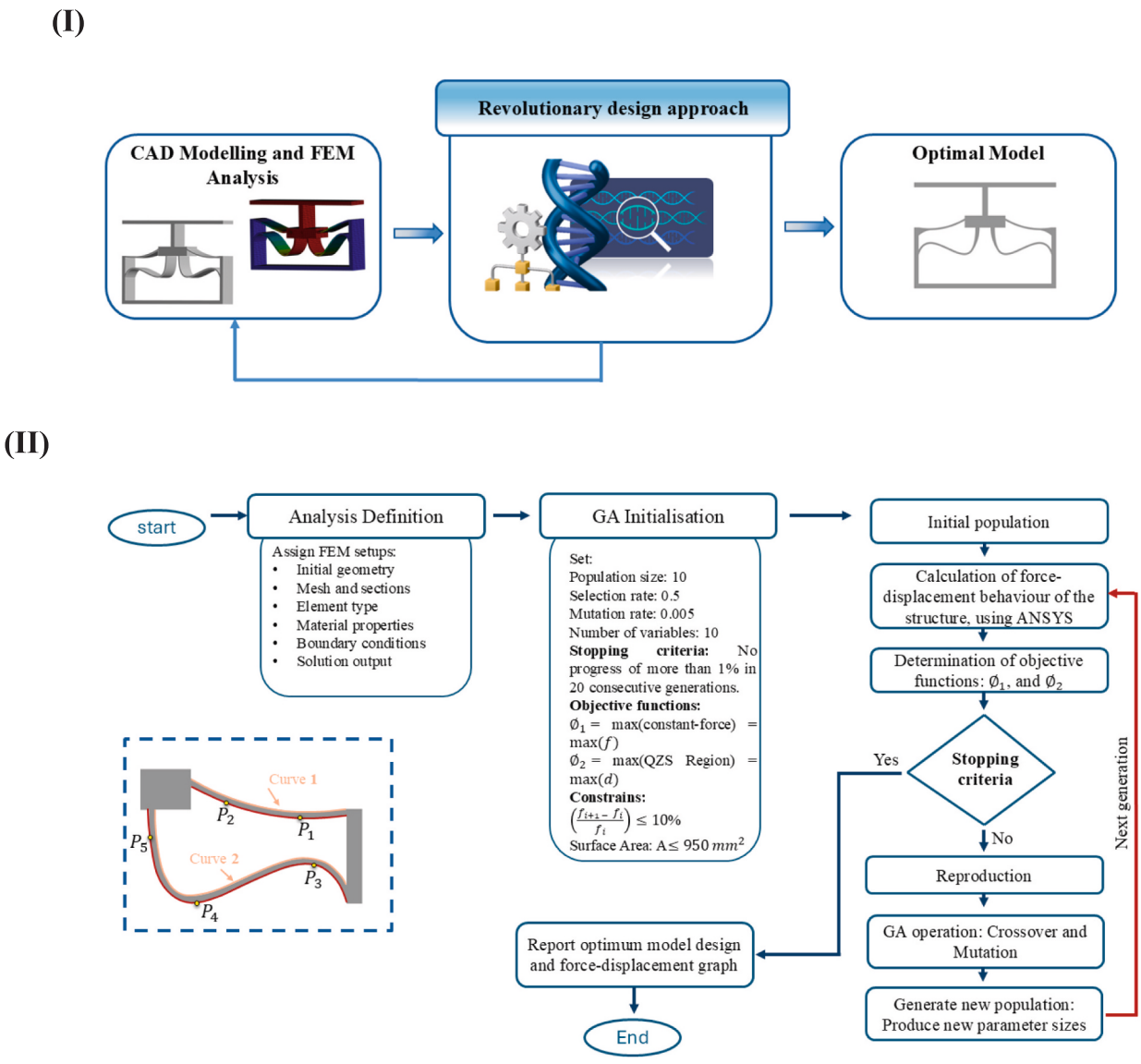

Fig. 3. (I) A schematic illustration of AI-assisted design. (II) The flowchart detailing the implementation of the multi-GA process.

Table 3
Controlling parameters with their specified changing range.

Parameter	Range
P_1	P_x(24:32), P_y(26:20)
P_2	P_x(12:20), P_y(19:23)
P_3	P_x(16:32), P_y(8:12)
P_4	P_x(7:14), P_y(3:7)
P_5	P_x(1:5), P_y(12:20)

Table 4
Specification of the developed multi-GA procedure.

Multi-GA properties	Value
Algorithm	Multi-objective GA
Number of iterations used	164
Execution time for each iteration (Minutes)	100
Convergence time (Minutes)	17,200
Algorithm's output	$\emptyset_1$ = 1.15 N, $\emptyset_2$= 5 mm

Table 5
3D printing factors utilised during the fabrication process.

Parameters	Value
Nozzle temperature (°C)	235
Bed temperature (°C)	60
Infill density (%)	100
Nozzle diameter (mm)	0.4
Layer thickness (mm)	0.2
Printing speed (mm/s)	40

composite material, with the reported mechanical properties reflecting the average data derived from these five results. Fig. 4(I) illustrates the printed dog-bones along with their geometric dimensions. Tensile tests were performed on samples according to the ASTM-D-638 Type-I standard at a speed of 5 mm/min, as depicted in Fig. 4(II).

Furthermore, dog-bone samples were evaluated under various cycling conditions to assess their mechanical responses during loading/unloading, relaxation, and reloading scenarios. Therefore, tests involving three cyclic loadings and cyclic stress-relaxation control were conducted. In the cyclic test with three loadings, the dog-bone sample

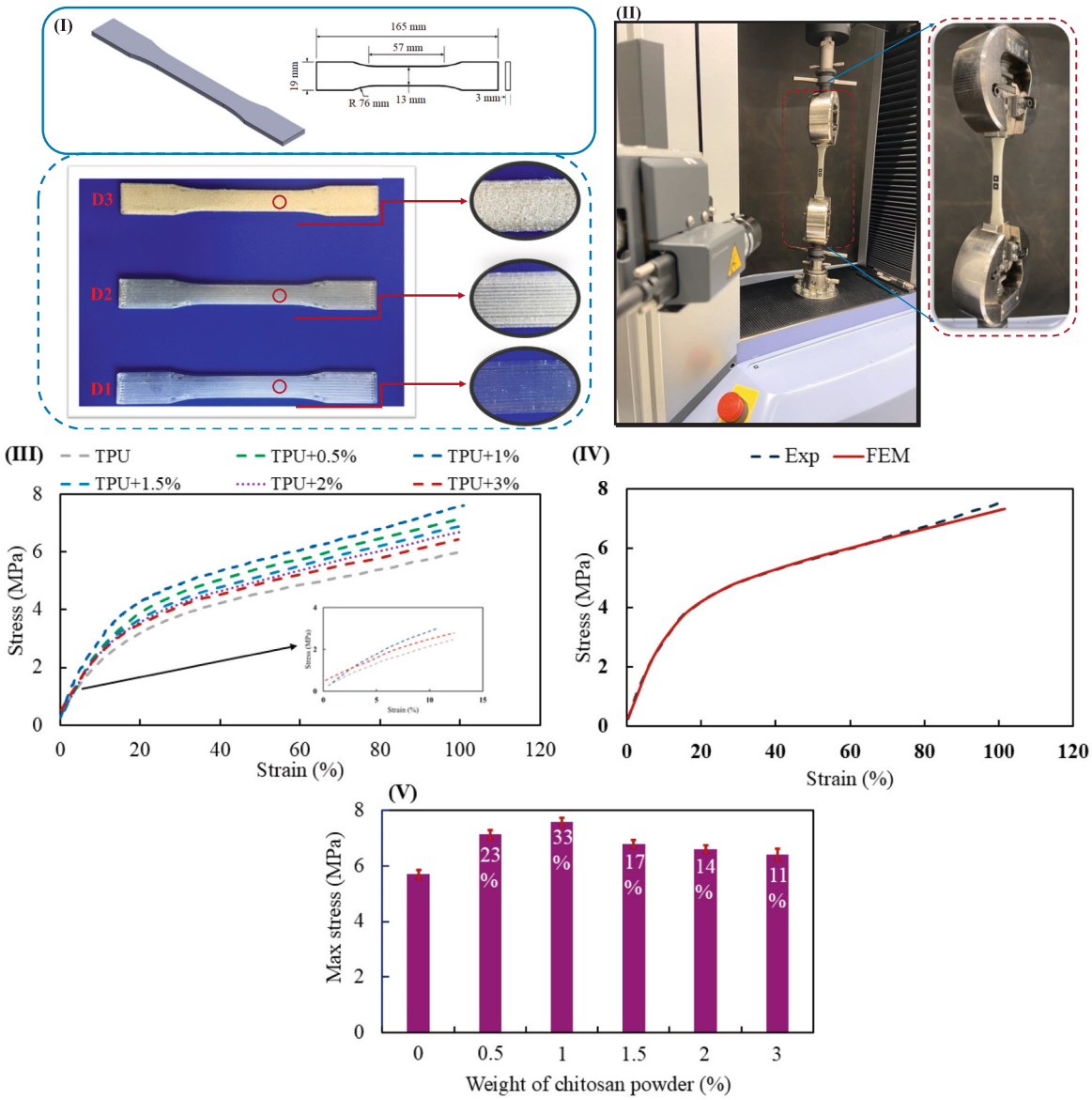

Fig. 4. Illustration of 3D-printed dog-bone samples made from reinforced bio-composites, along with their tested mechanical properties. (I) displays the fabricated samples, with D3, D2, and D1 representing TPU + 3 % CH, TPU + 1 % CH, and TPU bio-composites, respectively. The zoomed images highlight the surface quality of the prints, and the dimensions of the dog-bone samples are specified. (II) illustrates the experimental tensile test setup. (III) compares the stress-stiffness behaviour of the 3D-printed bio-composites, showing that TPU + 1 % CH exhibits greater stiffness than other alternatives. (IV) demonstrates that the FEM results align well with the experimental findings, validating the proposed FEM approach. (V) indicates that the addition of Chitosan powder enhances the stiffness, respectively. The red error bar shows the deviation range in the experimental data. (For interpretation of the references to colour in this figure legend, the reader is referred to the web version of this article.)

was subjected to strains of 50 %, 100 %, and 150 % at a speed of 5 mm/min. The two ends of the dog-bone were connected to screw action grips, with the top end being pulled by the testing machine while the bottom end remained fixed. In the cyclic stress-relaxation control test, the dog-bone sample was initially stretched by 8 mm (80 % strain) and then allowed to rest for 180 s. This was followed by an additional stretch of 1 mm, after which the sample rested for another 180 s. This cycle was repeated five times before the sample was unloaded, with all loadings executed at a speed of 5 mm/min. The residual strain for each sample was recorded after a resting period of 24 h. Similarly, five dog-bone samples were 3D printed and tested for each material, with the reported mechanical properties reflecting the average data derived from these five results.

In addition, the proposed QZS meta-structures were investigated under both monotonic and cyclic compression loadings to evaluate their force–displacement and energy dissipation characteristics. For the monotonic compression test, a compression displacement of 12 mm was applied to the top surface, with the stiffening walls supported by a printed cage to simulate fixed boundary conditions (refer to Fig. 11). The compression test was conducted at a consistent speed of 5 mm/min. In the case of the cyclic test, the meta-samples were subjected to a compression displacement of 13 mm at the same speed, followed by an unloading phase.

2.7. Wettability test

In various applications, such as sports equipment (e.g., running shoes, helmets, protective pads and gears) and healthcare (e.g., surgical instruments, rehabilitation devices, exercisers, bedding), the use of lightweight materials with high moisture (e.g., sweat) retention is

essential. Therefore, the developed composites underwent a wettability test to assess their water and moisture-holding levels. The wettability test was conducted using the optical tensiometer (Theta Lite). A material sample was placed on the testing bed, and a water drop with a volume of 5 μL was introduced onto its surface via an injector. Meanwhile, a CCD camera captured the data, which was subsequently processed using the OneAttension software package.

2.8. Flammability test

Flame resistance is critical for safety in various applications, including protective gears and wearable devices. The flammability characteristics of the three composites were thoroughly investigated using the Underwriters Laboratories (UL-94) horizontal burning test. The procedure applied is detailed below.

To evaluate the flammability of the samples, ASTM D635-22 standards [58] was followed, assessing the burning rate in a horizontal alignment. Printed samples positioned horizontally were placed in a fume hood and marked at distances of 25 mm and 100 mm from one end. A gas burner was then utilised to apply heat to the sample's end, allowing the flame to penetrate to a depth of 6 mm, at which point timing commenced. The time taken and distance travelled by the flame from the 25 mm mark to the 100 mm mark were recorded. In addition, a FLIR camera (FLIR E5-XT model with 19.200 (160 × 120) pixel infrared detector and expanded, −20 °C to 400 °C temperature range) was used to capture heat map images of the samples as they burned. The burning rate of the composites was subsequently calculated using the following equation:

$$S = \frac{60 \times l}{t} \tag{1}$$

where S indicates the burning rate (mm/min), l stands for the burned length (mm), and t denotes the burning time (*seconds*).

3. FEM simulations

ANSYS software was used to numerically calculate mechanical properties, utilising FEM as the primary solving tool. To calibrate the FEM before metamaterial simulations, a dog-bone sample according to ASTM-D-638 Type I was first 3D printed from TPU with 1 % CH and then tested experimentally. The experimental stress/strain data were imported into ANSYS. A nonlinear hyper-elastic material model was selected for the numerical analysis, as the fabricated bio-composites exhibited hyper-elasticity (see Fig. 4). A thorough investigation was conducted to assess the accuracy of existing hyper-elastic solving models, comparing the results with experimental data. Ultimately, the hyper-elastic Mooney-Rivlin model with five parameters was selected for simulations under monotonic loading. Following this calibration, the dog-bone was simulated and subjected to a monotonic loading replicating the boundary conditions used in the experimental test. In the mesh study, the mesh refinement technique (MRT) was employed with a constant-force convergence of 1 %. The chosen mesh type was a hexahedral mesh with an element size of 0.5 mm.

Additionally, the proposed QZS meta-structures were investigated numerically to evaluate their force–displacement behaviour, mode shapes, and energy dissipation characteristics under both monotonic and cyclic loadings. For the monotonic loading scenario, the FEM simulation was executed within the structural static domain using the hyper-elastic Mooney-Rivlin model with five parameters. In contrast, the cyclic analysis involved conducting FEM simulation in the transient structural domain, using a visco-hyper-elastic material model incorporating the Mooney-Rivlin five-parameter model along with the Prony series. The same boundary conditions employed in the experimental setup were consistently applied in these analyses.

4. Results and discussion

This section begins by highlighting the enhancement of material properties in the proposed reinforced bio-composite when compared to the pure TPU. Key aspects include tensile strength (under both monotonic and cyclic loading), hysteresis energy dissipation, wettability, and flame retardancy. Additionally, the force–displacement behaviour of the designed QZS metamaterials is examined and compared, utilising various material combinations across different loading conditions.

4.1. Mechanical characteristics of bio-composites

The tensile strength and stress–strain behaviours of 3D-printed bio-composites made from TPU reinforced with Chitosan particles at weight percentages of 0 %, 1 %, and 3 % were evaluated in accordance with ASTM D638-Type I standards (as illustrated in Fig. 4). The results from the experimental tensile tests indicate that incorporating 1 % Chitosan particles into the TPU considerably enhances tensile strength and improves the material's stiffness. However, further increases in Chitosan content from 1 to 3 % results in a reduction in tensile strength (refer to Fig. 4(III) and (V)). To indicate that the uncertainties in the experimental values fall within acceptable ranges, the standard deviation (SD) is reported for each set of averaged experimental data. To demonstrate that 1 % Chitosan reinforcement offers superior mechanical performance compared to other mixing options, we also examined the mixing percentages of 0.5 %, 1.5 %, and 2 %. The results presented in Fig. 4(III) and (V) indicate that the stiffness values decrease with both lower and higher additions of 1 % Chitosan.

The maximum stress observed at 100 % strain was 5.8 MPa (with 0.25 SD) in pure TPU, 7.15 MPa (with 0.28) in TPU with 0.5 % CH, 7.7 MPa (with 0.3 SD) in TPU with 1 % CH, 6.8 MPa (with 0.3) in TPU with 1.5 % CH, 6.6 MPa (with 0.31) in TPU with 2 % CH, and 6.42 MPa (with 0.33 SD) in TPU with 3 % CH. This indicates that strength increased by 33 % in TPU + 1 %CH and by 11 % in TPU + 3 %CH when compared to pure TPU. Fig. 4(I) displays the 3D-printed dog-bone samples, along with a zoomed-out view showcasing the printed surface quality. Based on the mechanical test results (Fig. 4(III)) and the SEM results, which shows the microstructural quality of the samples printed (Fig. 7), two possible explanations for this phenomenon emerge: 1) an excessive amount of Chitosan particles may compromise filament uniformity, leading to issues in the printing process that hinder the production of high-density samples; 2) aggregation of Chitosan particles may result in the formation of clusters within the TPU matrix, causing partial separation of micro-voids between particles and the composite. It disrupts stress transfer when tensile force is applied. Furthermore, a comparison was conducted between the stress–strain behaviour of TPU with 1 % Chitosan determined through experimental and numerical analyses. Fig. 4(IV) demonstrates that the developed FEM analysis is valid and generates results that align with the experimental data with less than 5 % deviation in the large strain of 100 %. Consequently, the FEM calibrated with these experimental test data has been employed to simulate the structural behaviour of meta-bio-composites in the following sections.

The stress–strain characteristics of 3D printed reinforced bio-composites were examined under various cyclic loading conditions, including stress-relaxation control and strain control, in accordance with ASTM D638-Type I standards. Fig. 5(I) to (III) illustrate the variation in strain as a function of time, reflecting the strain-control implementation within the cyclic testing for TPU, TPU + 1 %CH, and TPU + 3 %CH, respectively. The dog-bone samples were subjected to stretches of 50 %, 100 %, and 150 %, respectively. Fig. 5 demonstrates the loading, unloading, and reloading conditions as well as the residual strain.

Additionally, Fig. 5(IV) to (VI) present the stress–strain behaviour of the bio-composites under cyclic tensile loading at 50 %, 100 %, and 150 % strain increments, corresponding to TPU, TPU + 1 %CH, and TPU + 3

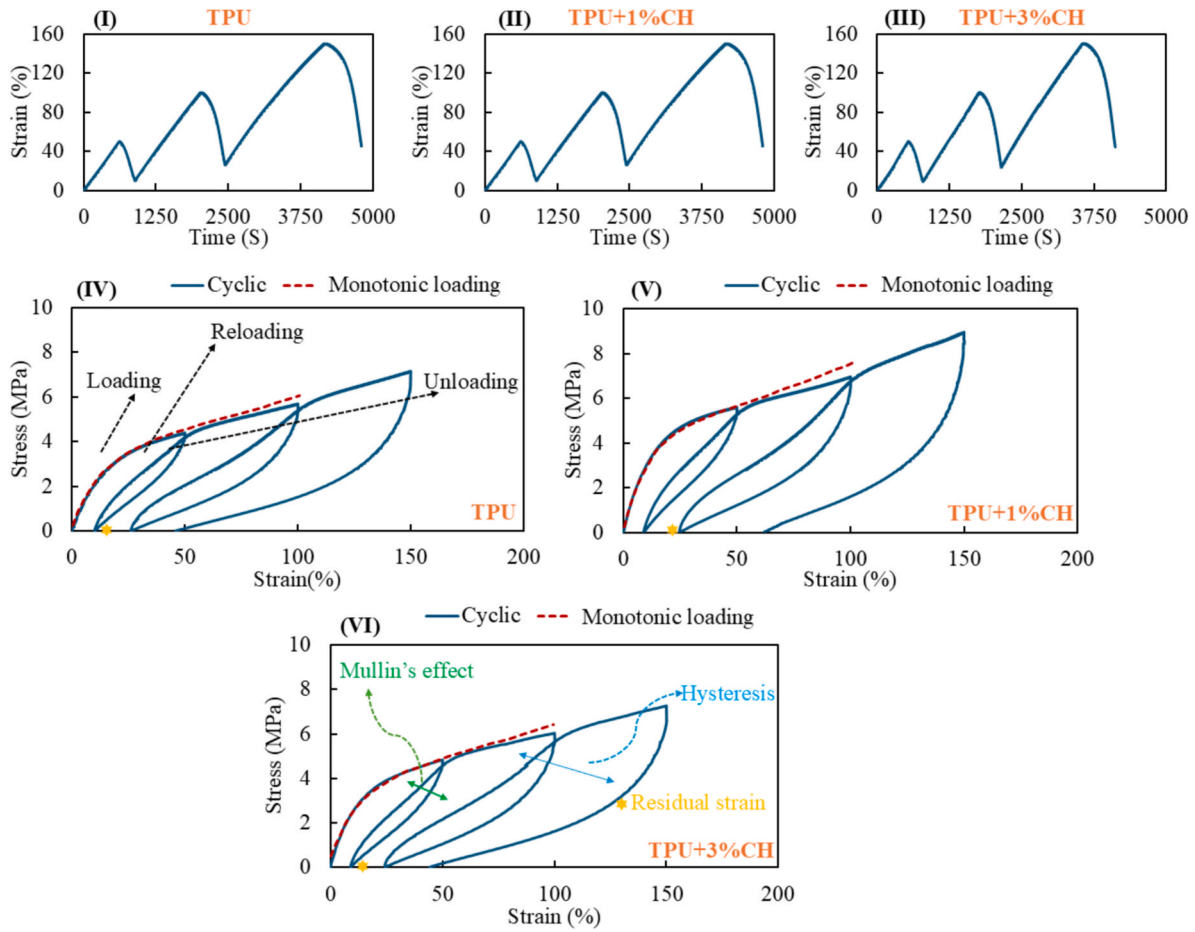

Fig. 5. Strain-controlled cyclic loading. (I) illustrates the strain changes as a function of time for the TPU case. (II) depicts the strain variations over time for the TPU + 1 %CH case. (III) presents the strain changes over time for the TPU + 3 %CH case. (IV) demonstrates the stress–strain behaviour of TPU under cyclic loading. (V) illustrates the stress–strain behaviour of TPU + 1 %CH during cyclic loading, while (VI) shows the stress–strain behaviour of TPU + 3 %CH under similar conditions. The dashed red line illustrates the stress–strain behaviour under monotonic loading. The results indicate that TPU + 1 %CH exhibits superior stiffness and enhanced energy dissipation compared to the other composites. (For interpretation of the references to colour in this figure legend, the reader is referred to the web version of this article.)

%CH, respectively. Notably, it is found that the TPU + 1 %CH composite demonstrated an increased stress level of 9 MPa, 6.9 MPa, and 5.71 MPa at 150 %, 100 %, and 50 % strain, respectively. In comparison, the stress levels for TPU + 3 %CH at 150 %, 100 %, and 50 % strain were 7.17 MPa, 6 MPa, and 4.82 MPa, respectively, while pure TPU showed values of 7.1 MPa, 5.5 MPa, and 4.4 MPa at the same strain levels. This indicates that the addition of 1 % Chitosan significantly enhances the material's stiffness under cyclic loading conditions.

Furthermore, the collective surface area under the three loading conditions is observed to be greater in both TPU + 1 %CH and TPU + 3 %CH composites compared to the pure TPU. The addition of Chitosan particles appears to enhance energy dissipation properties and enlarge the areas of hysteresis loops. Calculations reveal that the total energy dissipated over three cycles increased by 36 % (with 0.32 SD) for TPU + 1 %CH and by 15 % (with 0.35 SD) for TPU + 3 %CH when compared to pure TPU. After resting for 24 h post-test, TPU + 1 %CH had a residual strain of 22 % (with 0.28 SD), while TPU + 3 %CH had 17 % (with 0.26 SD), and the pure TPU exhibited 15 % (with 0.25 SD). A comparison of Fig. 5(IV), (V), and (VI) reveals that the Mullins effect, which involves stiffness reduction, is less pronounced in the TPU + 1 %CH composite compared to the TPU + 3 %CH and pure TPU samples. This is evidenced by the reduced distance between loading and reloading paths when 1 % Chitosan was added. The Mullin's effect arises from material damage due to repeated loading and unloading cycles, leading to softening and an irreversible reduction in stiffness. Consequently, a lower stress level is required for the same strain during subsequent loading (i.e., reloading) compared to the initial loading condition.

In practical applications, it is crucial for the constant-force mechanism to endure multiple loading/unloading cycles, requiring a reduction of the Mullins effect. The TPU + 1 %CH formulation has effectively reduced this undesired phenomenon. Furthermore, the FEM analysis of the bio-composites under monotonic loading, illustrated with a red dashed line (Fig. 5), demonstrates an acceptable correlation with the cyclic loading experimental results. The minor discrepancies observed after the initial loading can be attributed to stress reduction in the material during the reloading process.

We conducted a further investigation into the impact of loading rate on the stress–strain behaviour under cyclic tensile loading, utilising strain increments of 50 %, 100 %, and 150 %. For this purpose, three distinct loading rates were considered: 1 mm/min, 5 mm/min, and 10 mm/min. The TPU + 1 %CH composite was subjected to cyclic loading to evaluate the sensitivity of hysteresis and energy dissipation properties with respect to loading rate. As illustrated in Fig. A3, our findings revealed that higher loading rates correspond to an increase in peak stresses, attributed to rate-dependent strengthening, diminished plastic deformation, and a steeper cyclic stress–strain curve. It is evident that a faster loading rate results in higher stress levels with less hysteresis. This phenomenon occurs because the material lacks sufficient time to relax, leading to a stiffer response and consequently higher stress for the same strain. Moreover, concerning energy dissipation (hysteresis) that arises

from internal friction due to viscous flow and molecular rearrangement, at elevated loading rates, molecular chains cannot move freely, resulting in reduced internal friction and less time for energy loss mechanisms to take effect. Therefore, the material exhibits a more elastic response, as indicated by a narrower hysteresis loop. For instance, the experimental test demonstrated that increasing the loading rate from 1 mm/min to 10 mm/min elevates stress levels while producing steeper cyclic stress–-strain curves and reduced hysteresis loops. The stress levels recorded at 50 % and 100 % strain were 4.81 MPa and 5.73 MPa for the 1 mm/min loading rate, 5.71 MPa and 6.9 MPa for the 5 mm/min loading rate, and 6.24 MPa and 7.43 MPa for the 10 mm/min loading rate. Additionally, the analysis indicated that the total energy dissipated over three cycles increased by 8 % (with a standard deviation of 0.27) and 21 % (with a standard deviation of 0.30) for the 5 mm/min loading rate compared to the 10 mm/min and 1 mm/min loading rates, respectively. In conclusion, in isothermal cyclic tests, increasing loading rate generally leads to smaller hysteresis loops and less energy dissipation.

Furthermore, Fig. 6 illustrates the stress–strain characteristics of bio-composites subjected to cyclic loading with stress relaxation. It is evident that TPU + 1 %CH can endure higher stress levels and demonstrates superior energy dissipation compared to the other samples (see Fig. 6(II) and (IV)). It is noteworthy that the maximum stress observed in TPU with 1 % CH is 8.9 MPa, while in TPU with 3 % CH, it is 8.2 MPa. In contrast, the maximum stress in pure TPU is only 4.7 MPa. This reveals that pure TPU experiences a significant loss of stiffness under cyclic stress relaxation, whereas the structural stiffness in TPU with 1 % CH is improved by approximately 100 %. Furthermore, Fig. 6 indicates that the dissipated energy per unit volume is as follows: 640 $M\frac{J}{m^3}$(with 0.34 SD) for TPU + 1 %CH, 615 $M\frac{J}{m^3}$ (with 0.36 SD) for TPU + 3 %CH, and 304 $M\frac{J}{m^3}$ (with 0.28 SD) for pure TPU. Consequently, TPU + 1 %CH demonstrates an increase in dissipated energy of over 110 %. Moreover, the variation of stress as a function of time indicates that reinforcing TPU with Chitosan improves the material's stiffness during the loading, unloading, and reloading steps. According to Fig. 6(IV), the area under the stress-time graph represents the stress impulse, which indicates the material's stiffness in terms of its ability to transfer a larger momentum per unit area. The findings revealed that the stress impulse for TPU + 1 %CH is 29.84 GPa·s (0.34 SD), while for TPU + 3 %CH it is 28.5 GPa·s (with 0.36 SD), and TPU alone has a stress impulse of 11.85 GPa·s (with 0.28 SD). Consequently, both TPU + 1 %CH and TPU + 3 %CH demonstrate improvements in stress impulse of 152 % and 140 %, respectively.

4.2. Microstructural properties

SEM was employed to examine the microstructural features of the extruded filaments as well as 3D printed bio-composites. Fig. 7 reveals a robust contact at the layer interfaces, with minimal voids, suggesting effective impregnation and wet-out in the samples. Remarkably, the interfaces and bonding between layers are more adhesive in the TPU + 1 %CH and TPU + 3 %CH composites. During tensile tests, sections of the matrix show signs of pulling and damage due to the applied tensile stress. However, Chitosan particles present at the interfaces contribute to stopping the layer-breakage phenomenon, effectively mitigating damage growth and enhancing the composite's resistance to failure. This phenomenon may account for an increased strength observed with the addition of Chitosan to the TPU matrix. Furthermore, the enhanced energy dissipation capability can be attributed to the chemical and mechanical interlocking between the TPU matrix and the Chitosan particles. The incorporation of Chitosan introduces interfaces within the TPU matrix, where frictional slippage occurs between TPU particles and the matrix under external loads. This leads to effective mechanical energy dissipation and improved damping properties of the bio-composites. One possible reason for the superior mechanical properties of TPU + 1 %CH compared to TPU + 3 %CH is that this increase in Chitosan particles may render the composite smoother, exacerbating the presence of defects and voids in the printed material. Consequently, during tensile tests, layer-breakage may propagate from these defects. Ultimately, Fig. 7 illustrates that both the 3D printing and filament-making processes achieve acceptable production quality.

4.3. Wettability characteristics

Fig. 8 displays the evolution of the contact angle (CA) as a function of time for three different TPU-based materials. It is evident that

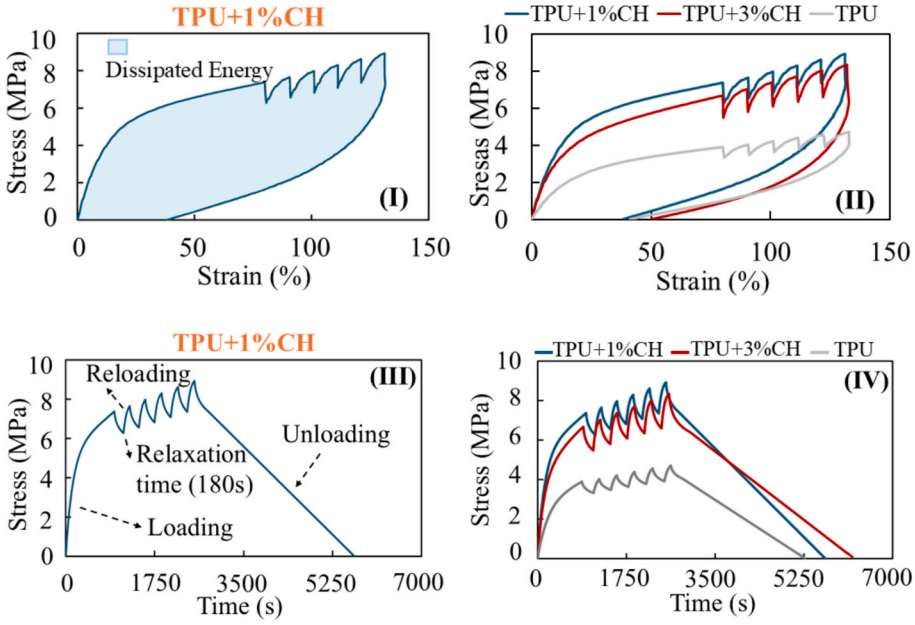

Fig. 6. Illustration of the stress-relaxation control under cyclic loading. (I) depicts the stress–strain behaviour and the dissapiated energy area of TPU + 1 %CH. (II) provides a comparison of the stress–strain behaviours of the three printed bio-composites. (III) shows the stress changes over time for TPU + 1 %CH (IV) compares the stress-time responses of the various 3D-printed bio-composites. The findings indicate that TPU + 1 %CH and TPU + 3 %CH display higher stiffness and energy dissipation levels compared to pure TPU, respectively.

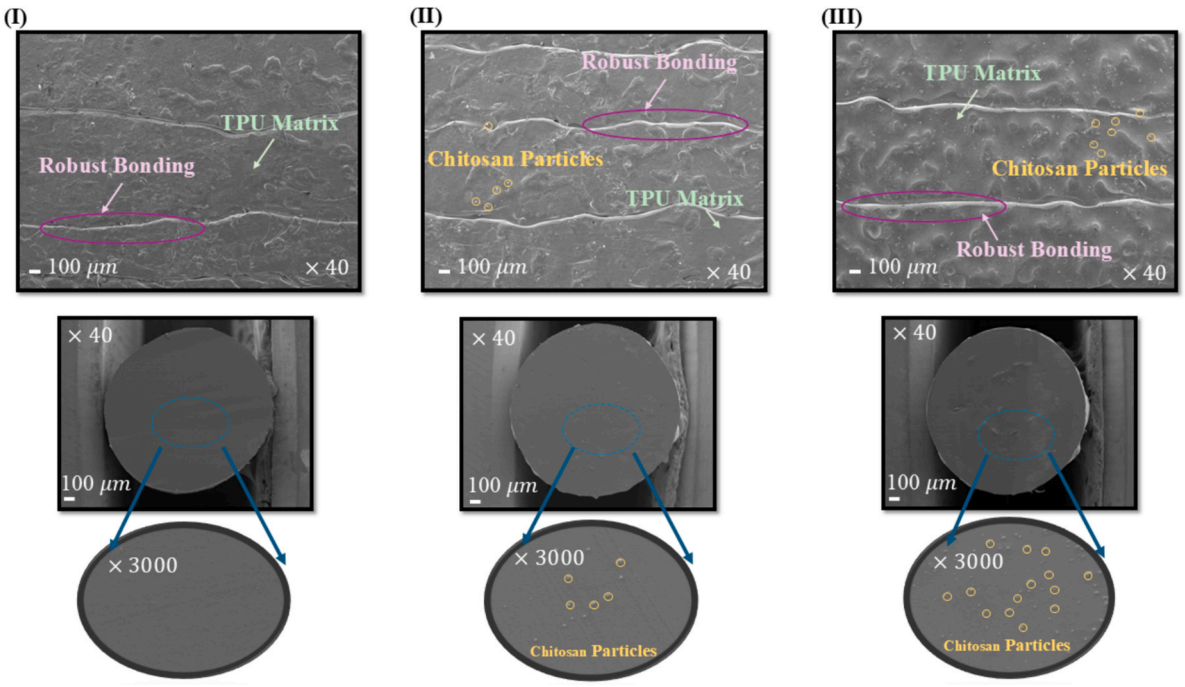

Fig. 7. Illustration of SEM microphotographs for 3D printed samples (first row) and filaments (second row). (I) corresponds to the pure TPU. (II) corresponds to the TPU + 1 %CH bio-composite, while (III) represents the TPU + 3 %CH bio-composite. It is evident that there is robust bonding between the layers in the samples, indicating the satisfactory quality of the 3D printing process. Additionally, the surface of the filament reflects the quality of the filament-making process, with Chitosan particles being uniformly distributed throughout.

incorporating Chitosan particles into the TPU matrix reduces the mean CA. Specifically, the addition of just 3 % Chitosan powder leads to a 13 % decrease in the mean CA, as well as a reduction in CA deviation over time. The study determined that the mean CA at the beginning was 74 deg for pure TPU, 69 deg for TPU + 1 %CH, and 64.5 deg for TPU + 3 % CH. After 10 s, the mean CA values were 69 deg for pure TPU, 65 deg for TPU + 1 %CH, and 59 deg for TPU + 3 %CH. It is noteworthy that both reinforced bio-composites showed a relatively constant mean CA after 6 s, while pure TPU continued to fluctuate until the end of the observation period. A lower mean CA indicates enhanced moisture retention properties. This observation can be attributed to the inherent characteristics of Chitosan, which offers moisture retention, better wettability, and hydrophilic properties. Chitosan, a biopolymer derived from chitin, has been extensively researched for its ability to retain moisture and hold water [59,60]. Notably, Chitosan is sourced from the shells of crustaceans, such as fish, crabs, prawns, and lobsters, which possess water-retaining capabilities.

The higher wettability and water retention properties make the proposed bio-composite valuable for sportswear such as shoe insoles, helmets, gym pads, and protective gears, and healthcare such as rehabilitation devices or exercisers where sweat-holding properties are desired. The average water CA of unmodified TPU, as reported in the literature, typically ranges from 70 to 95 degrees, indicating its moderately hydrophobic nature [61,62]. In this project, a CA of 74 deg was observed for the pure TPU, which aligns with the average range. It is important to note that this value can vary significantly with the incorporation of chemical additives or through surface modification techniques.

4.4. Flammability properties

The flammability characteristics of 3D-printed bio-composites were evaluated using the UL-94 horizontal burning test. Fig. 9 depicts the samples prior to testing, during combustion, and post-burning. The results indicate that the burning rate is reduced in reinforced samples. Adding 1 % and 3 % Chitosan results in a 32.5 % and 41.25 % decrease in burning rate, respectively. Table 6 presents the recorded burning rates for both pure and reinforced TPU fabrics. This reduction in burning rate can be attributed to the presence of natural Chitosan particles, which form protective layers that inhibit the penetration of heat and volatile substances into the inner layers of the composite. In essence, during thermal decomposition, Chitosan can create a char layer that insulates the material and curtails the spread of fire by limiting oxygen access to the burning surface, similar to the phenomenon observed in [63]. The findings underscore the excellent flame retardancy and thermal stability of 3D-printed Chitosan-based bio-composites. These properties are required in various application areas, e.g., sport, furniture, automotive, and aerospace applications like protection, safety, comfort gears exposed to fire/flame. Therefore, these fire-retardant bio-composites have the potential to promote a sustainable and safer product design paradigm.

4.5. Behaviours of QZS mechanical meta-structures

This section outlines the mechanical characteristics of two proposed QZS metamaterials featuring uniform and non-uniform curved layouts. The materials used for both experimental and numerical investigations are TPU + 1 %CH, TPU + 3 %CH, and pure TPU, with their properties determined in earlier sections. The influence of structural parameters on mechanical properties is illustrated in Fig. 10(I) to (III), derived from a comprehensive parametric study. This analysis enables us to identify the most influential geometric parameters prior to the optimisation implementation, thus minimising the number of geometrical factors considered in the optimisation analysis.

The results indicate that the thickness of the curved beams is critical to the mechanical properties, particularly in relation to the QZS region and the constant-force level. Fig. 10(III) illustrates the variation in QZS length and constant-force level as a function of the out-of-plane structure thickness (h). It is evident that increasing h reduces the QZS region while simultaneously increases the force level. This enhancement in

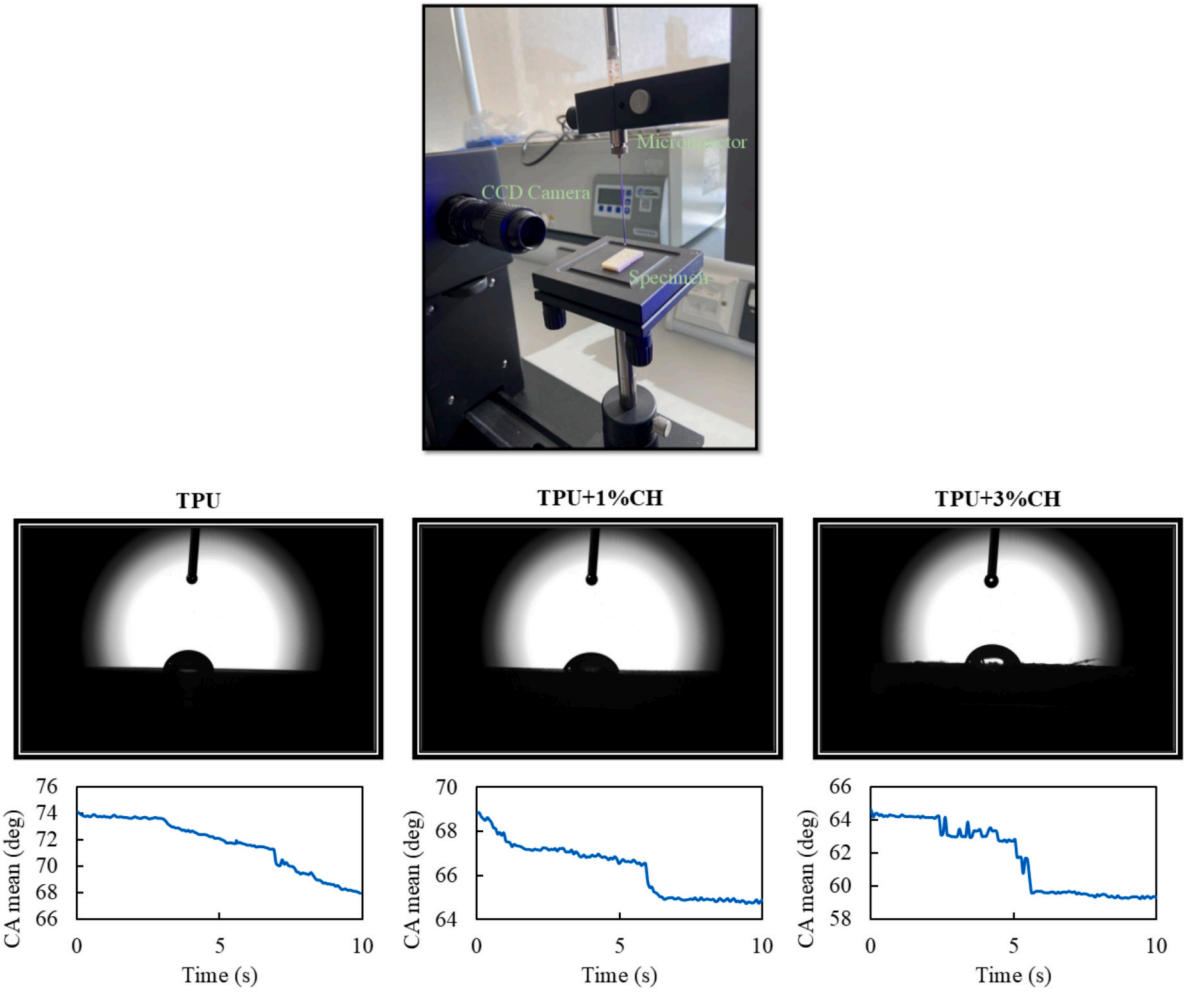

Fig. 8. Wettability experimental test setup, and the evolution of CA mean over time for TPU, TPU + 1 %CH, and TPU + 3 %CH. The study demonstrates that adding Chitosan particles decrease the CA, resulting in high wettability, and moisture-holding properties.

force capability can be attributed to the greater thickness of the structure, which allows it to better withstand applied compression forces. Furthermore, a multi-GA analysis was conducted on the uniform QZS meta-structure with the objective of simultaneously expanding the QZS region and enhancing the constant-force level. The AI-assisted design proposed a novel non-uniform curved metamaterial that showcases improved QZS properties, as depicted in Fig. 10(IV). It is noticeable that the curve thickness increases in regions of maximum stress concentration. In the subsequent study, the mode shapes are investigated to validate our findings. Furthermore, the optimisation plot is presented in Fig. 10(V), indicating that the two objective functions are maximised to 1.15 N and 5 mm, respectively.

Furthermore, to gain a better understanding of the relationship between the structural parameters and mechanical properties, polynomial regression was employed to establish correlations between the constant-force value and two key geometric parameters, t_1 and t_2. Similarly, a mathematical correlation was developed between the QZS length and the same geometric parameters. Correlations were formulated using data obtained from the parametric analysis. These correlations enhance the programmability and controllability of the system's mechanical performance. The coefficient of determination R^2 was found to be approximately 0.82 and 0.98 for the constant-force and QZS length correlations, respectively. Although R^2 is relatively acceptable, the high degree of nonlinearity in both geometric and material characteristics renders the correlations complex and less precise in capturing finer details. The established correlations are expressed as follows:

$$f_{QZS} = c_1 + a_1 t_1 + a_2 t_2 + a_3 t_1^2 + a_4 t_1 t_2 + a_5 t_2^2 + a_6 t_1^3 + a_7 t_1^2 t_2 + \cdots \left(uptot_1^{10}\right), \tag{2}$$

$$L_{QZS} = c_2 + b_1 t_1 + b_2 t_2 + b_3 t_1^2 + b_4 t_1 t_2 + b t_2^2 + b_6 t_1^3 + \cdots (uptot_1^6) \tag{3}$$

where f_{QZS} and L_{QZS} are the constant-force and the QZS length, respectively. Table 7 summarises the specifications and variable values of these nonlinear correlations. The corresponding plots are provided in the Appendix, where the trends of QZS length and constant-force values as functions of frame and curve thicknesses can be observed. Similar trend observed in Fig. 10(I) and 10(II), from Figs. A1(I) and A1(II) it can be observed that the constant-force level is maximised around 1.4 to 1.5 mm for t_2 and 1.1 mm for t_1. Regarding to the QZS length it is maximised around$t_1 = 1.1$ mm while t_2 varies. A similar trend to that observed in Fig. 10(I) and 10(II) can be identified in Figs. A2(I) and A2(II). It can be seen that the constant-force level reaches its maximum when t_2 is approximately 1.4–1.5 mm and t_1 is around 1.1 mm. With respect to the QZS length, the maximum value is attained at$t_1 = 1.1$ mm, while variations in t_2 influence the overall response.

Fig. 11 illustrates the 3D printed metamaterials by TPU, TPU + 1 % CH, and TPU + 3 %CH, along with the specified boundary conditions implemented in both experimental and numerical analyses. To investigate the mechanical properties of the variable thickness curved QZS metamaterial and to compare these properties under using different materials, experimental and FEM studies were conducted under varying monotonic and cyclic loading conditions. It is worth mentioning that to

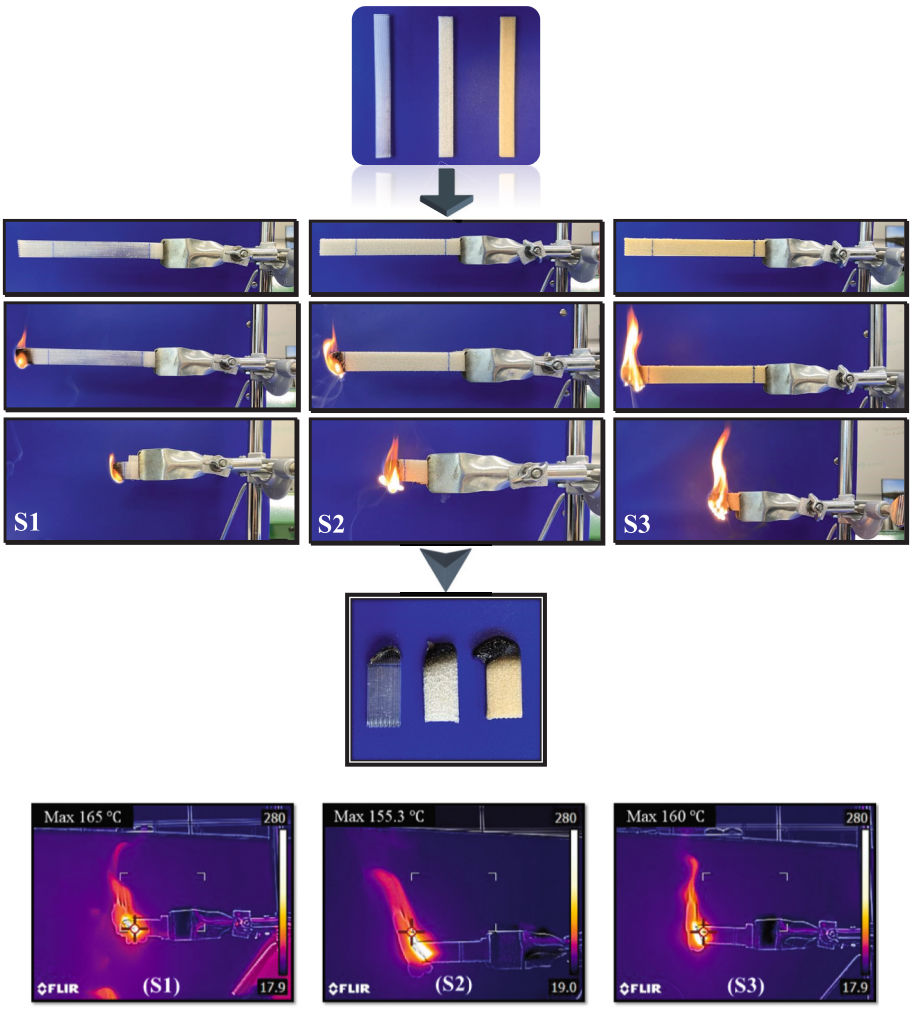

Fig. 9. Schematic representation of the flammability test setup, including the test procedure and post-burning evaluation. S1, S2, and S3 represent the TPU, TPU + 1 %CH, and TPU + 3 %CH samples, respectively.

Table 6
Flammability test outcomes.

Sample	Burning rate (mm/min)
TPU	40
TPU + 1 %CH	27
TPU + 3 %CH	23.5

minimise the influence of manufacturing and printing variations on the mechanical properties, five meta-samples were produced and tested for each composite material. The reported mechanical properties reflect the average data obtained from these five meta-samples. The force–displacement response of the proposed optimal QZS metamaterial is depicted in Fig. 12 for different bio-composites. The results indicated that TPU + 1 %CH can enhance the constant-force level and program its level in a wider range for a single unit-cell. Also, the comparison of Fig. 12(II) with Fig. 2(III) indicates that the optimisation study can enhance the QZS region and constant-force level by 67 % and 130 %, respectively. The optimal QZS metamaterial now produces values for the plateau region and the constant-force level of approximately 5 mm and 1.15 *N*, respectively. Notably, the force level and plateau length can be programmed based on the structural size, with values ranging from 0.5 N to 1.15 N and 1 to 5 mm, respectively.

Furthermore, an extensive analysis was performed on the samples to evaluate the accuracy of various nonlinear material solution models. The studied material solving models are: hyper-elastic Monney Rivlin five (H-MR5), and two parameters (H-MR2), visco-hyper-elastic Mooney Rivlin five parameters in conjunction with Prony series (VH-MR5), Yeoh three parameters (H-Yeoh3), and Neo-Hooken. The findings indicated that both the VH-MR5 and H-MR5 models closely matched the experimental results during single loading, showing less than a 3 % deviation from the experimental data. In contrast, the H-MR2, H-Yeoh3, and Neo-Hookean models exhibited errors exceeding 145 %.

Consequently, the VH-MR5 was applied for the FEM cyclic analysis, while the VH-MR5 was employed for the monotonic compression loading analysis to streamline the simulation process. Fig. 12(IV) compares the properties of the QZS metamaterial derived from the three different materials: TPU, TPU + 1 %CH, and TPU + 3 %CH. It was seen that incorporating 1 % Chitosan enhanced the structural strength and resulted in an improvement of approximately 130 % in the constant-force level, shifting it from 0.5 to 1.15 N, while the plateau region remained unchanged.

Besides, the mode shapes of the proposed non-uniform curved QZS metamaterial were examined through both experimental and numerical compression analyses. Fig. 13 illustrates that the mode shapes obtained from the FEM are consistent with those observed in the experimental study. The numerical analysis indicates that the maximum strain reached approximately 11 %, underscoring the importance of large deformation modelling for this structure under the specified loading conditions. 2D contour plot in Fig. 13 visually represents strain distribution and reveals that the peak strain occurs in the connecting sections

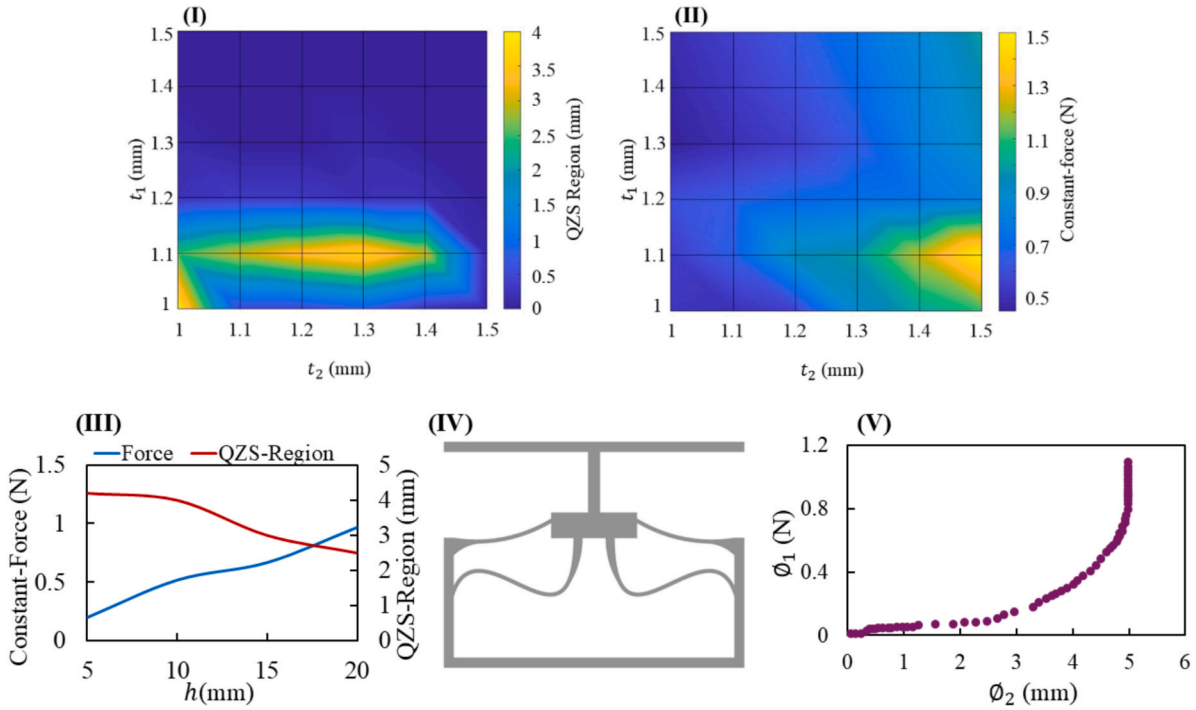

Fig. 10. Illustration of the results from the Parametric and Optimisation analysis. (I) and (II) explain the influence of frame thickness and curve thickness on the length of the plateau region and the constant-force level, respectively. (III) depicts the variation in the QZS region length and the constant-force level as a function of out-of-plane structure thickness. (IV) showcases the optimised QZS metamaterial featuring non-uniform curved beams. (V) presents the outcome of the multi-GA analysis, indicating that the maximum QZS length and constant-force level are 5 mm and 1.15 *N*, respectively.

Table 7
Values of factors used in the nonlinear correlations between mechanical properties and geometry parameters.

f_{QZS} variables	Values (mm)	L_{QZS} variables	Values (mm)
c_1	0.638	c_2	20222.3161
a_1	3.1×10^{-5}	b_1	−30287.6387
a_2	-1.81×10^{-5}	b_2	−29763.9478
a_3	7.47×10^{-5}	b_3	−16132.5038
a_4	1.18×10^{-5}	b_4	71893.8149
a_5	-4.24×10^{-5}	b_5	−14719.3549
a_6	1.36×10^{-5}	b_6	11043.5349
a_7	5.36×10^{-5}	_	_

The authors declare that they have no known competing financial interests or personal relationships that could have appeared to influence the work reported in this paper.

of the curves, validating the findings of the optimisation study. This suggests that those areas possess critical influence, and their shape and thickness should be optimised to enhance both the QZS region and the constant-force level.

In addition, the QZS behaviour of the proposed meta-structure was investigated under cyclic loading both through experimental and numerical approaches. Fig. 14 presents the cyclic force–displacement responses of the system using different material compositions. Energy dissipation values were derived from the corresponding force–displacement curves, yielding 18 *N*.mm (with 0.27 SD) for TPU + 1 % CH, 14.52 *N*.mm (with 0.28 SD) for TPU + 3 %CH, and 10.2 *N*.mm (with 0.22 SD) for pure TPU. Therefore, it is proven that 1 % and 3 % reinforcement with Chitosan can enhance the energy dissipation by 77 % and 43 %, respectively.

The incorporation of 1 % Chitosan into the TPU matrix results in a broader cyclic hysteresis, indicating enhanced energy dissipation compared to other configurations. Both reinforced composites demonstrate increased energy dissipation and higher force levels relative to the unreinforced TPU, confirming the role of Chitosan in improving mechanical performance. The reason TPU with 1 % Chitosan exhibits higher energy dissipation compared to TPU with 3 % Chitosan is that the incorporation of more than 1 wt% of Chitosan powder can lead to increased brittleness and reduced interlayer adhesion. As a result, the negative effects of higher Chitosan content gradually outweigh the positive benefits on structural strength and energy dissipation properties. Furthermore, consistent constant-force behaviour is observed during both loading and unloading phases. The cyclic loading tests were performed over five consecutive cycles, during which no observable stiffness degradation (i.e., Mullins effect) was detected. As shown in Fig. 14, this stability under repeated loading suggests that the meta-structure is capable of sustaining multiple cycles without a decline in energy dissipation and constant-force performance. Such repeatability is essential for many practical applications—such as shoe insoles—where the structure is exposed to thousands of loading/unloading cycles daily, while its QZS characteristics must remain reliably preserved. Indeed, this meta-structure with QZS properties has promising potential for applications in low-frequency vibration isolation. For this purpose, a weight equivalent to the constant force can be added to the top of the meta-structure to adjust the structure in the QZS region. Meanwhile, the lower layer would be subjected to low-frequency vibrations. Consequently, the meta-structure has the ability to diminish vibration waves and effectively isolate vibration energy through the QZS mechanism [34,36]. Additionally, the QZS mechanical feature of the proposed metamaterial was graphically compared with several available structures, as displayed in Fig. A3. It has been observed that the designed meta-structure shows an enhanced QZS length while maintaining a relatively small structural size.

In an extended investigation, two optimal metamaterial unit cells were configured in an intersecting arrangement to form a multi-unit cell, or supercell, meta-structure. This configuration was considered to address applications requiring the close spatial integration of multiple unit cells in a more scalable and potentially 3D layout. The intersected geometry was designed to ensure positional stability of the metamaterial

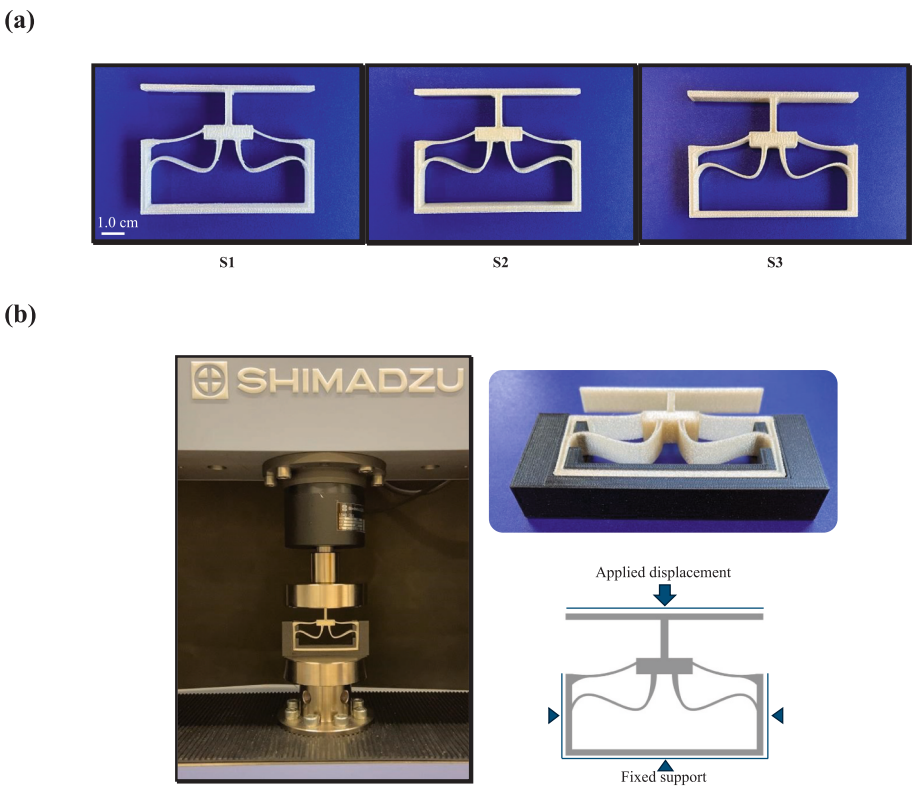

Fig. 11. Schematic illustration of: a) the 3D printed optimum QZS specimens, where S1, S2, and S3 stand for TPU, TPU + 1 %CH, and TPU + 3 %CH, respectively. b) displays the experimental and FEM compression test setup along with the applied boundary conditions.

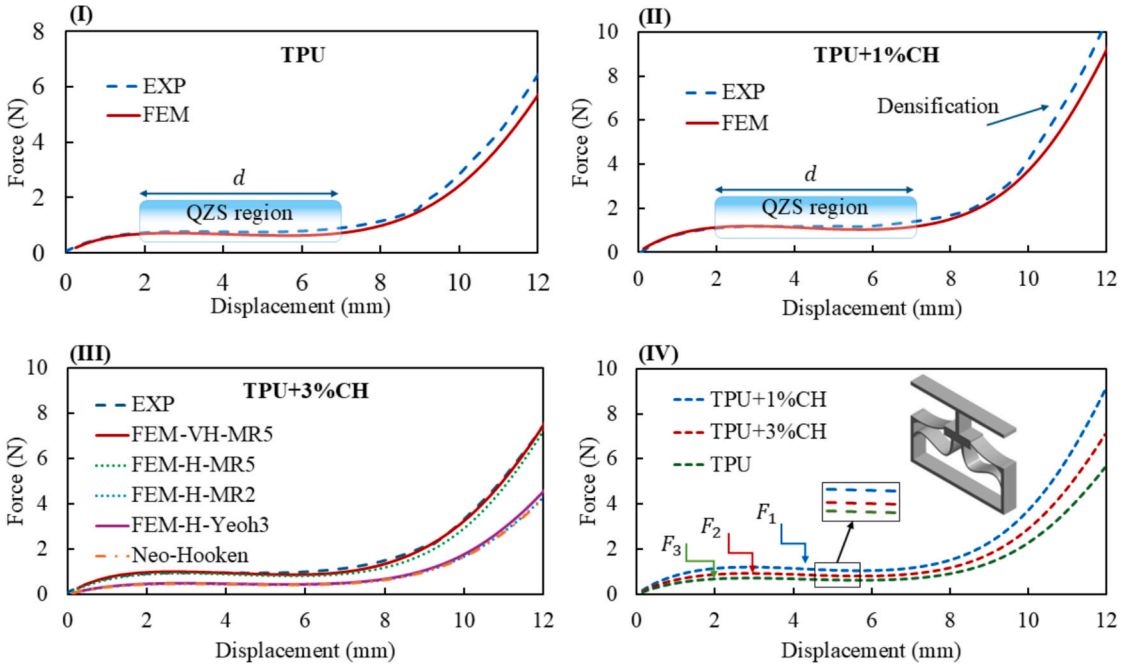

Fig. 12. Demonstrating the force–displacement response of optimal QZS metamaterial using different materials, as calculated from experimental and FEM studies. (I) corresponds to the TPU case study. (I) refers to the TPU + 1 %CH case study. (III) corresponds to the TPU case study and includes a comparison of force–displacement results obtained from different nonlinear material solution methods. (IV) compares the force–displacement characteristics of three bio-composites, focusing on the QZS region and constant-force levels.

units without the need for external support structures. The constant-force behaviour of the crossed configuration was evaluated through compression tests conducted under defined boundary conditions. As shown in Fig. 15, the results indicate that the supercell maintain an equivalent QZS region while approximately doubling the output force (2.21 N), a direct consequence of the dual-unit cell setup. This architecture provides a tuneable strategy for tailoring the force response to meet specific functional demands. Furthermore, the strain distribution

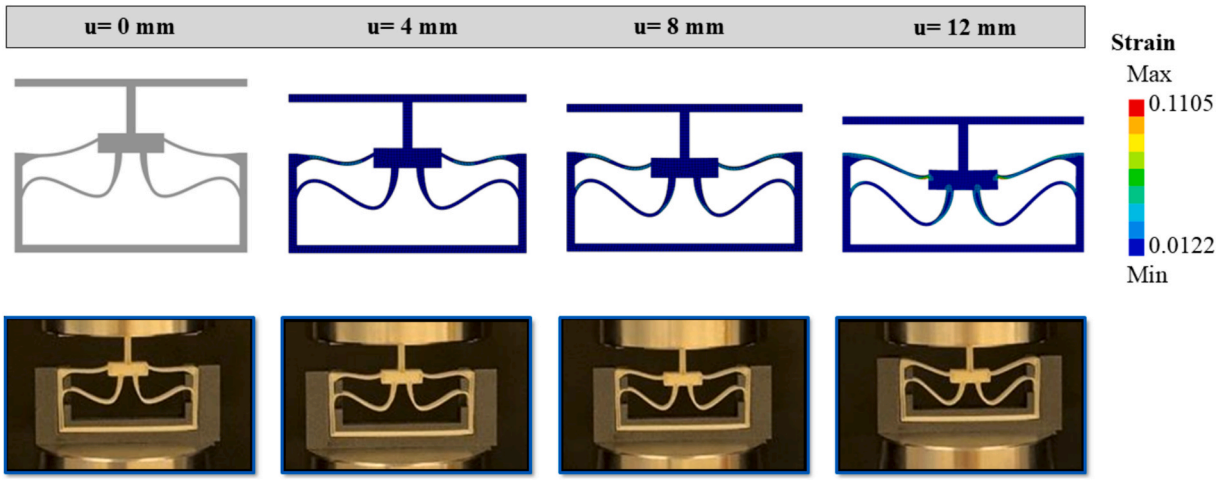

Fig. 13. Displaying the mode shapes of the AI-assisted QZS metamaterial during compression test. The mode shapes obtained from experimental and FEM analysis show good agreement, illustrating the accuracy of FEM studies.

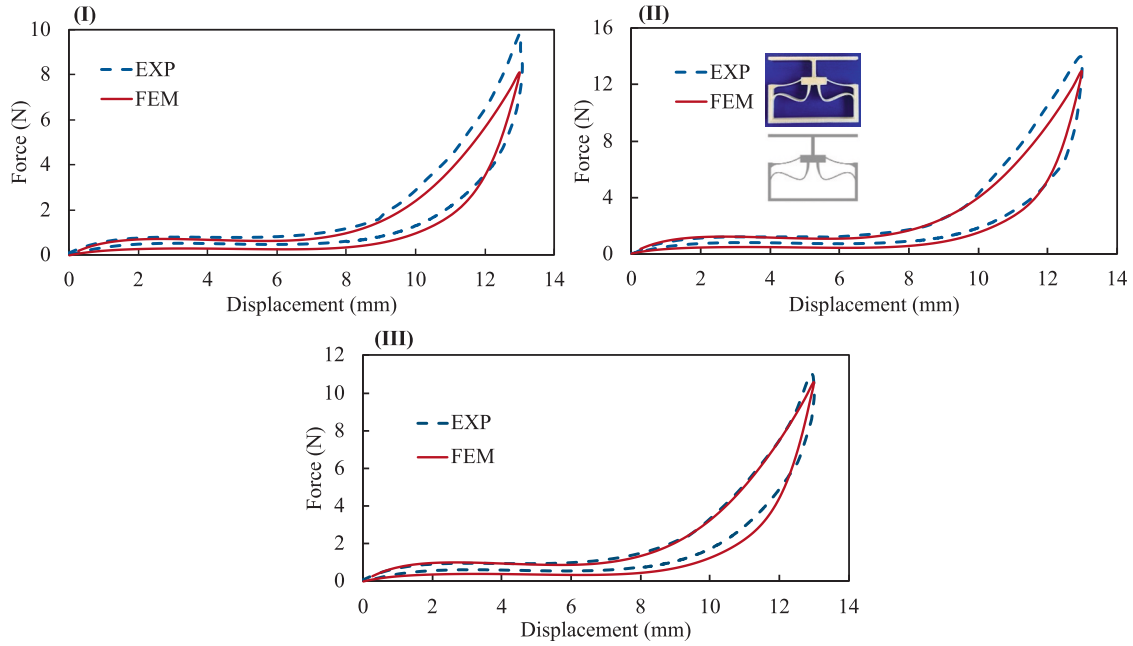

Fig. 14. Presentation of cyclic force–displacement behaviour of the proposed QZS metamaterial. (I) corresponds to the case study with TPU. (II) corresponds to the case study with TPU + 1 %CH. (III) corresponds to the case study with TPU + 3 %CH. It is observed that TPU + 1 %CH yields a higher constant-force level and greater energy dissipation compared to other combinations.

in the contour plot reveals an increased maximum strain of 0.182 (65 % increment), suggesting enhanced load-bearing capacity under elevated stress levels. Such modular and repeatable designs are essential for transitioning QZS metamaterials from single-plane prototypes to more complex, application-specific 3D constructs.

5. Potential applications

The proposed QZS metamaterial demonstrates promising potential for practical implementation due to its combination of structural tunability and multifunctional material performance. Capable of delivering a controllable QZS under deformation, the developed metamaterials can effectively absorb and dissipate elastic energy while the force level is kept constant. This behaviour also promotes safety and comfort as the meta-device does not let the impacting/touching object experience excessive force/stress. These QZS and constant-force features would make them ideal for applications where energy dissipation, impact mitigation, mechanical adaptability, overload protection, safety and comfort are critical or/and desired. In addition to its bio-inspired geometry, the integration of Chitosan-reinforced TPU introduces enhanced flame retardancy, moisture retention, and mechanical strength. Importantly, the material exhibits antibacterial properties [64], which are highly beneficial in applications involving prolonged skin contact or exposure to sweat or liquid, such as sportswear, home and automotive furniture, and medical devices. Together, these synergistic properties make the proposed metamaterial highly suitable for a wide range of applications—including wearable devices, protective equipment, and high-stress components across industries such as healthcare, sports, furniture, automotive, and aerospace.

Imagine a scenario in which a single metamaterial platform could enhance the human experience from toe to head—supporting movement, enabling recovery, and improving protection through everyday

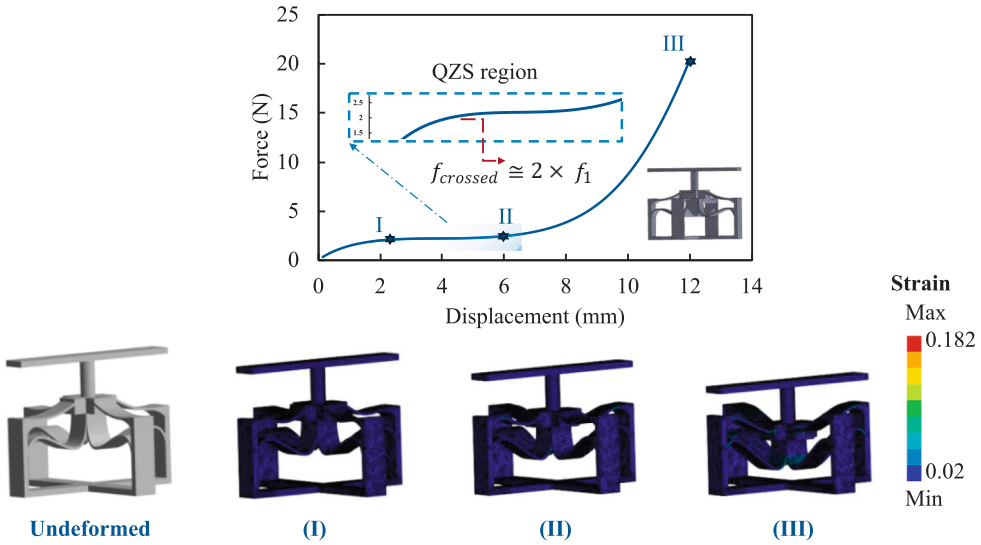

Fig. 15. Force–displacement response of the crossed-shape metamaterial structure. The multi-unit cell configuration exhibits QZS characteristics while generating a force level approximately twice that of a single-unit cell design.

wearables. In shoe insoles, the proposed QZS metamaterial can absorb energy and deliver a stable constant-force response over displacements up to 5 mm (studied here but can be extended by the proposed methodology), reducing pressure on the foot. This is particularly beneficial for individuals with diabetes or rheumatic conditions, where localised pressure, shock, or uneven load distribution can cause discomfort, joint inflammation or foot ulceration. By providing gentle and adjustable support and a customisable force profile, the metamaterial insole design is likely to locally alleviate pain, improve gait, and reduce the adverse impact on soft tissues and joints not only in the affected foot but lower limb joints, including knees and hips during weight bearing. It will also provide an opportunity for patients to find comfortable footwear for an unmet medical need. Moving upward, the QZS metamaterial can be integrated into hand exercisers or rehabilitation grips, delivering a consistent resistance profile ideal for physical therapy or muscle conditioning. The constant-force behaviour ensures smooth and fatigue-resistant motion, which is particularly beneficial for users with reduced grip strength or joint stiffness. The meta-structure would support recovery from injury or managing chronic musculoskeletal conditions like arthritis, where controlled muscle activation and joint relief are critical. At the upper end, in protective helmets, the QZS meta-structure acts as an energy absorber/dissipator and over-load protector that mitigates impact forces while retaining a compact form factor. This makes it suitable for sports and industrial applications, where safety and comfort must co-exist. A visual summary of these application domains is presented in Fig. 16.

Apart from unique structural features, crucially, the material itself also offers a suite of performance-enhancing properties. Its higher wettability and moisture retention facilitate effective sweat absorption, thereby maintaining skin comfort and reducing the risk of heat rash. The

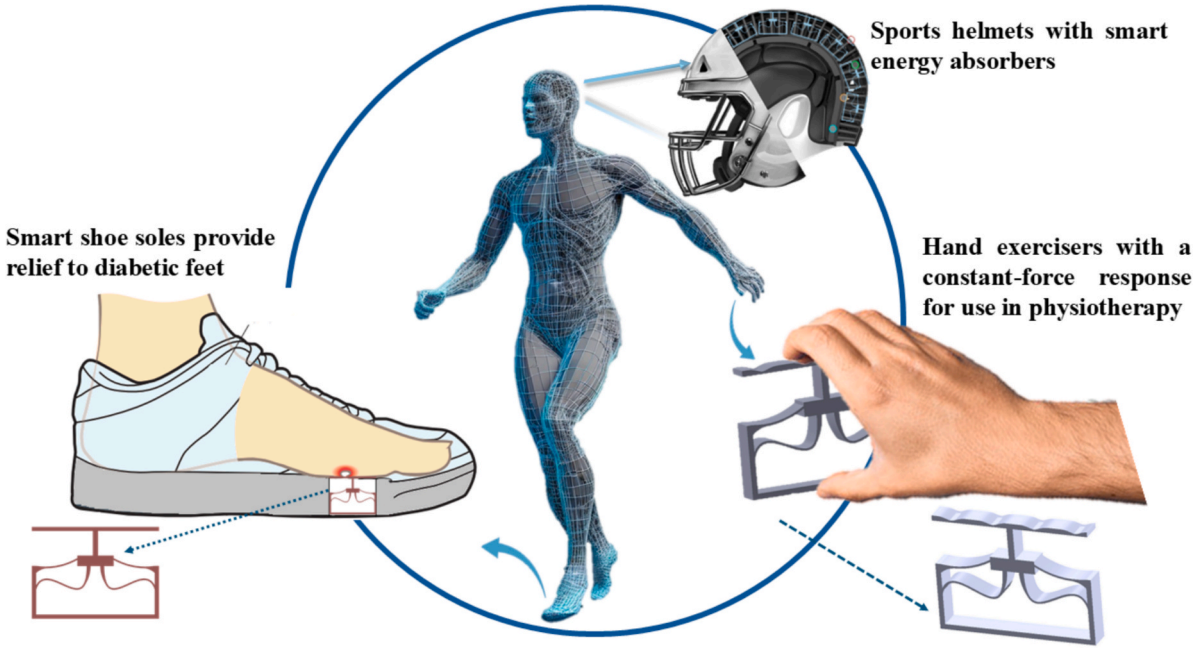

Fig. 16. Illustration of potential application domains for the proposed QZS metamaterials, including wearable/medical devices and protective equipment across sports, healthcare, and mobility sectors.

inclusion of Chitosan provides antibacterial action and odour control, making it desirable for extended use in high-activity or warm environments. Furthermore, it demonstrates flame-retardant behaviour, adding a critical layer of thermal safety—particularly valuable in applications such as helmets, gloves, or home/vehicle furniture/interiors, where exposure to heat or ignition sources is a concern. These features, in combination with the structure's mechanical adaptability, result in a metamaterial that is not only functionally robust but also hygienically, thermally, and ergonomically suited to a wide array of real-world scenarios. It is important to note that both the constant-force level and the structural size can be tailored by adjusting the geometric aspect ratio, allowing the design to be adapted for specific use cases across various industries.

6. Concluding Remarks

This study introduces a novel multifunctional QZS metamaterial platform, integrating coral-inspired curvilinear architectures with sustainable, reinforced bio-composites. A hybrid design strategy, combining visco-hyper-elastic FEM-based simulation and AI-guided optimisation, enabled precise control over the plateau region and constant-force output. A TPU matrix reinforced with 1 wt% Chitosan was identified as optimal for simultaneously enhancing mechanical strength and energy dissipation, along with flame retardancy, and moisture retention. Experimental and numerical results confirmed stable QZS behaviour, repeatable hysteresis loops, and negligible Mullins effect under cyclic loading. Conclusions on materials and metamaterials are summarised as follows:

- Mechanical performance: Reinforcing TPU with 1 % Chitosan increased tensile strength by 33 % and enhanced energy dissipation by 110 %.
- Impulse capacity: Stress impulse increased by 152 % with 1 % chitosan, improving the material's momentum transfer capability under cyclic loading.
- Burning resistance: Flame retardancy improved, with 1 % and 3 % Chitosan reducing the burning rate by 32.5 % and 41.25 %, respectively.
- Moisture retention: 3 % Chitosan increased wettability, improving moisture retention by 13 % – valuable for hygiene-critical, sweat-prone applications.
- Cyclic durability: Five-cycle tests confirmed stable force–displacement behaviour with no detectable stiffness degradation, indicating suppression of Mullins effect in the 1 % Chitosan-reinforced system, and long-term structural integrity.
- Numerical agreement: FEM simulations using visco-hyper-elastic models showed high fidelity with experimental tests, validating the modelling framework.
- Optimised metamaterial geometry: FEM-RL design achieved a 5 mm plateau region with a tuneable constant-force response between 0.5 and 1.15 *N*.
- Scalability: An interconnected dual-unit cell architecture doubled the constant-force output while maintaining QZS characteristics.

Fig. 17 summarises the main material and metamaterial improvements in this study. This multifunctional metamaterial platform addresses critical limitations in force regulation, overload protection, comfort, hygiene, and sustainability. The programmable mechanical behaviour, coupled with embedded antibacterial, moisture-regulating, and flame-retardant features, makes it highly suitable for next-generation orthopaedic devices, rehabilitation grips, and protective sports gear across healthcare, sports, and mobility sectors.

7. Future perspective

In future research, attention will be directed towards investigating the potential of the proposed QZS structure for low-frequency vibration reduction. Since low-frequency vibrations often result in substantial displacement levels, it is expected that employing the proposed QZS metamaterial with its hyper-elastic bio-composite will facilitate the dissipation of vibrational energies to higher thresholds.

CRediT authorship contribution statement

Shawn Ravanbod: Writing – review & editing, Writing – original draft, Visualization, Validation, Software, Methodology, Investigation, Formal analysis, Data curation, Conceptualization. **Kaveh Rahmani:** Writing – review & editing, Methodology, Investigation, Data curation. **Sarah Karmel:** Writing – review & editing, Supervision, Methodology, Investigation. **Ira Pande:** Writing – review & editing, Supervision, Investigation. **Hoda Amel:** Writing – review & editing, Supervision, Methodology, Investigation. **Callum Branfoot:** Writing – review & editing, Supervision, Methodology, Investigation. **Arash M. Shahidi:** Writing – review & editing, Supervision, Methodology, Investigation. **Andrew Alderson:** Writing – review & editing, Validation, Supervision, Methodology, Investigation. **Mahdi Bodaghi:** Writing – review & editing, Writing – original draft, Validation, Supervision, Resources, Project

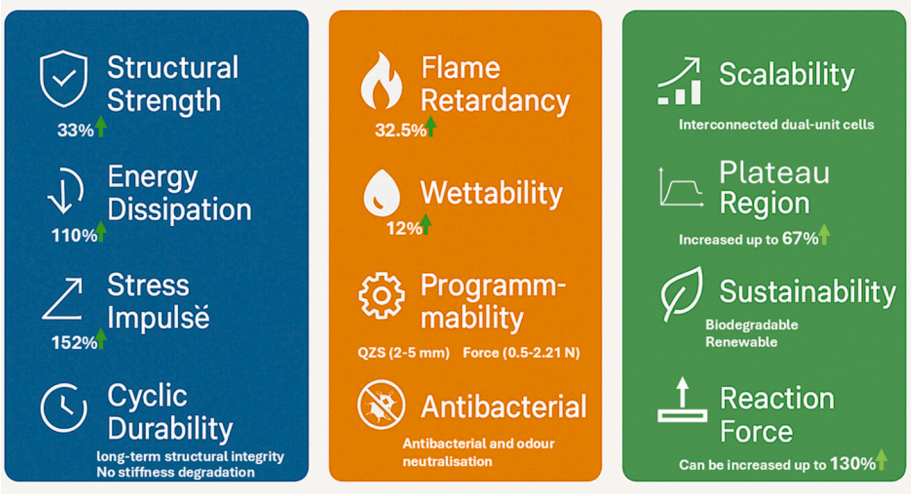

Fig. 17. Schematic illustration highlighting the key material and metamaterial advancements achieved in this study. The selected material is the bio-composite TPU reinforced with 1% chitosan, while the structural design features the proposed multifunctional, non-uniform curvilinear QZS metamaterial.

administration, Methodology, Investigation, Funding acquisition, Data curation, Conceptualization.

Declaration of competing interest

The authors declare that they have no known competing financial interests or personal relationships that could have appeared to influence the work reported in this paper.

Acknowledgements

The authors acknowledge the support by the Engineering and Physical Sciences Research Council (EPSRC) [I5M project, award number: EP/Y011457/1], and the EPSRC's Innovation Launchpad Network+ Researcher in Residence scheme [BIO-CYCLE project, grant numbers: EP/W037009/1, EP/X528493/1, award number: RIR26C230615-6, Researcher: Mahdi Bodaghi].

Appendix A. Supplementary data

Supplementary data to this article can be found online at https://doi.org/10.1016/j.matdes.2025.114398.

Data availability

Data will be made available on request.

References

[1] M. Jia, N. Dai, T. Wang, Q. Cao, L. Yan, H. Dai, A compact quasi-zero stiffness metamaterial for energy absorption and impact protection, Thin-Walled Struct. 205 (2024) 112360, https://doi.org/10.1016/j.tws.2024.112360.
[2] M. Shirzad, J. Kang, G. Kim, M. Bodaghi, S.Y. Nam, Bioinspired 3D-printed auxetic structures with enhanced fatigue behavior, Adv. Eng. Mater. 26 (20) (2024), https://doi.org/10.1002/adem.202302036.
[3] S. Guo, S. Liu, R. Gao, A bidirectional quasi-zero stiffness metamaterial for impact attenuation, Int. J. Mech. Sci. 268 (2024) 108998, https://doi.org/10.1016/j.ijmecsci.2024.108998.
[4] M. Ravanbod, S. Ebrahimi-Nejad, M. Mollajafari, A thin-walled cavity structure with double-layer tapered scatterer locally resonant metamaterial plates for extreme low-frequency attenuation, Int. J. Solids Struct. 293 (2024) 112742, https://doi.org/10.1016/j.ijsolstr.2024.112742.
[5] T.A.M. Hewage, K.L. Alderson, A. Alderson, F. Scarpa, Double-negative mechanical metamaterials displaying simultaneous negative stiffness and negative Poisson's Ratio properties, Adv. Mater. 28 (46) (2016) 10323–10332, https://doi.org/10.1002/adma.201603959[6] McHale, G., Alderson, A.
[6] S. Armstrong, S. Mandhani, M. Meyari, G.G. Wells, E. Carter, R. Ledesma-Aguilar, C. Semprebon, K.E. Evans, Transforming Auxetic metamaterials into superhydrophobic surfaces, Small Struct. 5 (4) (2024), https://doi.org/10.1002/sstr.202300458.
[7] S. Yan, W. Liu, X. Tan, Z. Meng, W. Luo, H. Jin, Y. Wen, J. Sun, L. Wu, J. Zhou, Bio-inspired mechanical metamaterial with ultrahigh load-bearing capacity for energy dissipation, Mater. Today 77 (2024) 11–18, https://doi.org/10.1016/j.mattod.2024.06.003.
[8] R. Lakes, K.W. Wojciechowski, Negative compressibility, negative Poisson's ratio, and stability, Physica Status Solidi (b) 245 (3) (2008) 545–551, https://doi.org/10.1002/pssb.200777708.
[9] G. Wang, T. Wang, Z. Chen, Z. Zhu, C.W. Lim, A novel 3D topological metamaterial for controllability of polarization-dependent multilayer elastic waves, Compos. B Eng. 275 (2024) 111341, https://doi.org/10.1016/j.compositesb.2024.111341.
[10] X. Fang, D. Yu, J. Wen, Y. Dai, M.R. Begley, H. Gao, P. Gumbsch, Large recoverable elastic energy in chiral metamaterials via twist buckling, Nature (2025), https://doi.org/10.1038/s41586-025-08658-z.
[11] H. Pu, J. Liu, M. Wang, J. Ding, Y. Sun, Y. Peng, J. Luo, Bio-inspired quasi-zero stiffness vibration isolator with quasilinear negative stiffness in full stroke, J. Sound Vib. 574 (2024) 118240, https://doi.org/10.1016/j.jsv.2024.118240.
[12] X. Xin, Z. Wang, C. Zeng, C. Lin, L. Liu, Y. Liu, J. Leng, 4D printing bio-inspired chiral metamaterials for flexible sensors, Compos. B Eng. 286 (2024) 111761, https://doi.org/10.1016/j.compositesb.2024.111761.
[13] S. Fang, K. Chen, Z. Lai, S. Zhou, D. Yurchenko, W.-H. Liao, A bio-inspired system for simultaneous vibration isolation and energy harvesting in post-capture spacecraft, Mech. Syst. Sig. Process. 199 (2023) 110466, https://doi.org/10.1016/j.ymssp.2023.110466.
[14] Y. Cui, H. Luo, T. Yang, W. Qin, X. Jing, Bio-inspired structures for energy harvesting self-powered sensing and smart monitoring, Mech. Syst. Sig. Process. 228 (2025) 112459, https://doi.org/10.1016/j.ymssp.2025.112459.
[15] J. Yi, R. Lyu, Y. Li, C. Wan, K. Zhang, Stability-enhanced variable stiffness metamaterial with controllable force-transferring path, Adv. Funct. Mater. 35 (4) (2025), https://doi.org/10.1002/adfm.202413789.
[16] C. Zhou, G. Sui, Y. Chen, X. Shan, A nonlinear low frequency quasi zero stiffness vibration isolator using double-arc flexible beams, Int. J. Mech. Sci. 276 (2024) 109378, https://doi.org/10.1016/j.ijmecsci.2024.109378.
[17] C. Zeng, L. Liu, Y. Hu, W. Zhao, X. Xin, Y. Liu, J. Leng, Stair-stepping mechanical metamaterials with programmable load plateaus, Adv. Funct. Mater. 34 (49) (2024), https://doi.org/10.1002/adfm.202408887.
[18] J. Tang, Y. Yang, Y. Li, D. Cao, A 6-DOF micro-vibration isolation platform based on the quasi-zero-stiffness isolator, Proc. Inst. Mech. Eng. C J. Mech. Eng. Sci. 235 (22) (2021) 6019–6035, https://doi.org/10.1177/09544062211010831.
[19] B.R. Krishnan, A.N. Biswas, K.V. Ahalya Kumar, P.S. Rama Sreekanth, Auxetic structure metamaterial for crash safety of sports helmet, Mater. Today Proc. 56 (2022) 1043–1049, https://doi.org/10.1016/j.matpr.2021.09.110.
[20] S. Zhou, P. Xu, B. Hou, Z. Ren, Dynamic characteristics analysis of bilayer bio-inspired X-shaped vibration isolation structure, Int. J. Non Linear Mech. 154 (2023) 104447, https://doi.org/10.1016/j.ijnonlinmec.2023.104447.
[21] P. Ling, L. Miao, W. Zhang, C. Wu, B. Yan, Cockroach-inspired structure for low-frequency vibration isolation, Mech. Syst. Sig. Process. 171 (2022) 108955, https://doi.org/10.1016/j.ymssp.2022.108955.
[22] G. Yan, W.-H. Qi, J.-J. Lu, F.-R. Liu, H. Yan, L.-C. Zhao, Z.-Y. Wu, W.-M. Zhang, Bio-inspired multi-joint-collaborative vibration isolation, J. Sound Vib. 568 (2024) 118089, https://doi.org/10.1016/j.jsv.2023.118089.
[23] G. Yan, H.-X. Zou, S. Wang, L.-C. Zhao, Z.-Y. Wu, W.-M. Zhang, Bio-inspired Vibration Isolation: Methodology and Design, Appl. Mech. Rev. 73 (2) (2021), https://doi.org/10.1115/1.4049946.
[24] R. Hamzehei, M. Bodaghi, N. Wu, Bio-inspired design and 4D printing of multi-stiffness wavy metamaterial energy absorbers/dissipators with shape recovery features, Eng. Struct. 327 (2025) 119538, https://doi.org/10.1016/j.engstruct.2024.119538.
[25] X. Zhou, H. Liu, J. Zhang, L. Ren, L. Zhang, Q. Liu, B. Li, C. Xu, L. Ren, 4D printed bio-inspired polygonal metamaterials with tunable mechanical properties, Thin-Walled Struct. 205 (2024) 112609, https://doi.org/10.1016/j.tws.2024.112609.
[26] G. Yan, H.-X. Zou, S. Wang, L.-C. Zhao, Z.-Y. Wu, W.-M. Zhang, Bio-inspired toe-like structure for low-frequency vibration isolation, Mech. Syst. Sig. Process. 162 (2022) 108010, https://doi.org/10.1016/j.ymssp.2021.108010.
[27] X. Sun, Z. Qi, J. Xu, Vibration properties of a knee bio-inspired nonlinear isolation structure, Int. J. Non Linear Mech. 147 (2022) 104245, https://doi.org/10.1016/j.ijnonlinmec.2022.104245.
[28] G. Yan, W.-H. Qi, J.-W. Shi, H. Yan, H.-X. Zou, L.-C. Zhao, Z.-Y. Wu, X.-Y. Fang, X.-Y. Li, W.-M. Zhang, Bionic paw-inspired structure for vibration isolation with novel nonlinear compensation mechanism, J. Sound Vib. 525 (2022) 116799, https://doi.org/10.1016/j.jsv.2022.116799.
[29] H. Fan, L. Yang, Y. Tian, Z. Wang, Design of metastructures with quasi-zero dynamic stiffness for vibration isolation, Compos. Struct. 243 (2020) 112244, https://doi.org/10.1016/j.compstruct.2020.112244.
[30] A. Carrella, M.J. Brennan, I. Kovacic, T.P. Waters, On the force transmissibility of a vibration isolator with quasi-zero-stiffness, J. Sound Vib. 322 (4–5) (2009) 707–717, https://doi.org/10.1016/j.jsv.2008.11.034.
[31] Y.-C. Wang, J.G. Swadener, R.S. Lakes, Anomalies in stiffness and damping of a 2D discrete viscoelastic system due to negative stiffness components, Thin Solid Films 515 (6) (2007) 3171–3178, https://doi.org/10.1016/j.tsf.2006.01.031.
[32] S. Zuo, D. Wang, Y. Zhang, Q. Luo, Design and testing of a parabolic cam-roller quasi-zero-stiffness vibration isolator, Int. J. Mech. Sci. 220 (2022) 107146, https://doi.org/10.1016/j.ijmecsci.2022.107146.
[33] G. Wen, J. He, J. Liu, Y. Lin, Design, analysis and semi-active control of a quasi-zero stiffness vibration isolation system with six oblique springs, Nonlinear Dyn. 106 (1) (2021) 309–321, https://doi.org/10.1007/s11071-021-06835-z.
[34] L. Xiao, X. Sun, L. Cheng, X. Yu, Broadband and robust vibration reduction in lattice-core sandwich beam with 3D-printed QZS resonators, Compos. Struct. 352 (2025) 118626, https://doi.org/10.1016/j.compstruct.2024.118626.
[35] K. Sun, J. Tang, Z. Wu, Y. Li, D. Cao, Coupled nonlinear vibration characteristics of quasi-zero-stiffness Gough-Stewart isolation platform, Aerosp. Sci. Technol. 152 (2024) 109352, https://doi.org/10.1016/j.ast.2024.109352.
[36] S. Dalela, B. PS, D.P. Jena, M. Leblouba, A tunable metamaterial using a single beam element with quasi-zero-stiffness characteristics for low-frequency vibration isolation, J. Vib. Control 30 (15–16) (2024) 3641–3658, https://doi.org/10.1177/10775463231198892.
[37] B. Ding, X. Li, S.-C. Chen, Y. Li, Modular quasi-zero-stiffness isolator based on compliant constant-force mechanisms for low-frequency vibration isolation, J. Vib. Control 30 (13–14) (2024) 3006–3020, https://doi.org/10.1177/10775463231188160.
[38] T. Liu, R. Deng, L. Jin, J. Cai, Rate-dependent and delayed snap-through behaviors of viscoelastic metamaterials, Int. J. Mech. Sci. 283 (2024) 109664, https://doi.org/10.1016/j.ijmecsci.2024.109664.
[39] S. Yan, Z. Meng, W. Liu, X. Tan, P. Cao, Y. Wen, Z. Xiang, J. Chen, Y. Xu, Y. Wang, J. Sun, L. Wu, J. Zhou, Self-contact snapping metamaterial for tensile energy dissipation, Mater. Horiz. 11 (24) (2024) 6352–6360, https://doi.org/10.1039/D4MH01013B.
[40] M. Bodaghi, W.H. Liao, 4D printed tunable mechanical metamaterials with shape memory operations, Smart Mater. Struct. 28 (4) (2019) 045019, https://doi.org/10.1088/1361-665X/ab0b6b.
[41] Q. Zhang, D. Guo, G. Hu, Tailored Mechanical Metamaterials with Programmable Quasi-Zero-Stiffness Features for Full-Band Vibration Isolation, Adv. Funct. Mater. 31 (33) (2021), https://doi.org/10.1002/adfm.202101428.

[42] W. Liu, L. Wu, J. Sun, J. Zhou, Tunable multifunctional metamaterial sandwich panel with quasi-zero stiffness lattice cores: load-bearing, energy absorption, and vibration isolation, Adv. Mater. Technol. 9 (4) (2024), https://doi.org/10.1002/admt.202301586.
[43] H. Hong, S. Kim, W. Kim, W. Kim, J. Jeong, S.S. Kim, Design optimization of 3D printed kirigami-inspired composite metamaterials for quasi-zero stiffness using deep RL learning integrated with bayesian optimization, Compos. Struct. 359 (2025) 119031, https://doi.org/10.1016/j.compstruct.2025.119031.
[44] W. Liu, S. Yan, Z. Meng, L. Wu, Y. Xu, J. Chen, J. Sun, J. Zhou, Programmable quasi-zero-stiffness metamaterials, Engineering (2024), https://doi.org/10.1016/j.eng.2023.11.027.
[45] J. Tang, T. Wang, Y. Li, H. Lin, H. Chen, D. Cao, Low-frequency band gap vibration isolation of local-resonant metamaterial beam with curved-beam resonators, Mech. Adv. Mater. Struct. 1–13 (2024), https://doi.org/10.1080/15376494.2024.2434196.
[46] A.R. Damanpack, M. Bodaghi, W.H. Liao, A robust hyper-elastic beam model under bi-axial normal-shear loadings, Int. J. Non Linear Mech. 95 (2017) 287–295, https://doi.org/10.1016/j.ijnonlinmec.2017.07.001.
[47] M. Lalegani Dezaki, R. Sales, A. Zolfagharian, H. Yazdani Nezhad, M. Bodaghi, Soft pneumatic actuators with integrated resistive sensors enabled by multi-material 3D printing, Int. J. Adv. Manuf. Technol. 128 (9–10) (2023) 4207–4221, https://doi.org/10.1007/s00170-023-12181-8.
[48] M. Bodaghi, A. Serjouei, A. Zolfagharian, M. Fotouhi, H. Rahman, D. Durand, Reversible energy absorbing meta-sandwiches by FDM 4D printing, Int. J. Mech. Sci. 173 (2020) 105451, https://doi.org/10.1016/j.ijmecsci.2020.105451.
[49] S. Rezaei, J. Kadkhodapour, R. Hamzehei, B. Taherkhani, A.P. Anaraki, S. Dariushi, Design and modeling of the 2D auxetic metamaterials with hyperelastic properties using topology optimization approach, Photonics Nanostruct. Fundam. Appl. 43 (2021) 100868, https://doi.org/10.1016/j.photonics.2020.100868.
[50] R. Hamzehei, J. Kadkhodapour, A.P. Anaraki, S. Rezaei, S. Dariushi, A. M. Rezadoust, Octagonal auxetic metamaterials with hyperelastic properties for large compressive deformation, Int. J. Mech. Sci. 145 (2018) 96–105, https://doi.org/10.1016/j.ijmecsci.2018.06.040.
[51] M. Bodaghi, K. Rahmani, M.L. Dezaki, C. Branfoot, J. Baxendale, 3D/4D printed bio-composites reinforced by bamboo charcoal and continuous flax fibres for superior mechanical strength, flame retardancy and recoverability, Polym. Test. 143 (2025) 108709, https://doi.org/10.1016/j.polymertesting.2025.108709.
[52] T.E. Baldock, H. Karampour, R. Sleep, A. Vyltla, F. Albermani, A. Golshani, D. P. Callaghan, G. Roff, P.J. Mumby, Resilience of branching and massive corals to wave loading under sea level rise – a coupled computational fluid dynamics-structural analysis, Mar. Pollut. Bull. 86 (1–2) (2014) 91–101, https://doi.org/10.1016/j.marpolbul.2014.07.038.
[53] M. Watanabe, H. Kan, K. Toguchi, Y. Nakashima, V. Roeber, T. Arikawa, Effect of the structural complexity of a coral reef on wave propagation: a case study from Komaka Island, Japan. Ocean Engineering 287 (2023) 115632, https://doi.org/10.1016/j.oceaneng.2023.115632.
[54] F. Ferrario, M.W. Beck, C.D. Storlazzi, F. Micheli, C.C. Shepard, L. Airoldi, The effectiveness of coral reefs for coastal hazard risk reduction and adaptation, Nat. Commun. 5 (1) (2014) 3794, https://doi.org/10.1038/ncomms4794.
[55] L. Pasquini, A. Molinari, P. Fantazzini, Y. Dauphen, J.-P. Cuif, O. Levy, Z. Dubinsky, E. Caroselli, F. Prada, S. Goffredo, M. di Giosia, M. Reggi, G. Falini, Isotropic microscale mechanical properties of coral skeletons, J. R. Soc. Interface 12 (106) (2015) 20150168, https://doi.org/10.1098/rsif.2015.0168.
[56] L.A. Melbourne, M.W. Denny, R.L. Harniman, E.J. Rayfield, D.N. Schmidt, The importance of wave exposure on the structural integrity of rhodoliths, J. Exp. Mar. Biol. Ecol. 503 (2018) 109–119, https://doi.org/10.1016/j.jembe.2017.11.007.
[57] S. Goffredo, A. Mancuso, E. Caroselli, F. Prada, Z. Dubinsky, G. Falini, O. Levy, P. Fantazzini, L. Pasquini, Skeletal mechanical properties of Mediterranean corals along a wide latitudinal gradient, Coral Reefs 34 (1) (2015) 121–132, https://doi.org/10.1007/s00338-014-1222-6.
[58] ASTM D635-Standard Test Method for Rate of Burning And/or Extent and Time of Burning of Plastics in a Horizontal Position, ASTM International, West Conshohocken, PA, USA, 2003.
[59] L. Liu, B. Wang, Y. Gao, T. Bai, Chitosan fibers enhanced gellan gum hydrogels with superior mechanical properties and water-holding capacity, Carbohydr. Polym. 97 (1) (2013) 152–158, https://doi.org/10.1016/j.carbpol.2013.04.043.
[60] L. Chen, Y. Du, H. Wu, L. Xiao, Relationship between molecular structure and moisture-retention ability of carboxymethyl chitin and Chitosan, J. Appl. Polym. Sci. 83 (6) (2002) 1233–1241, https://doi.org/10.1002/app.2290.
[61] D. Kanmaz, R. Celen, E. Karaca, G. Manasoglu, Investigation of wettability, thermal stability, and solar behavior of composite films based on thermoplastic polyurethane and barium titanate nanoparticles, Polymers 16 (23) (2024) 3259, https://doi.org/10.3390/polym16233259.
[62] A.G. Cullis, D.J. Norris, M.A. Migliorato, M. Hopkinson, Surface elemental segregation and the Stranski–Krastanow epitaxial islanding transition, Appl. Surf. Sci. 244 (1–4) (2005) 65–70, https://doi.org/10.1016/j.apsusc.2004.10.066.
[63] S. Hu, L. Song, Y. Hu, Preparation and characterization of chitosan-based flame retardant and its thermal and combustible behavior on polyvinyl alcohol, Polym.-Plast. Technol. Eng. 52 (4) (2013) 393–399, https://doi.org/10.1080/03602559.2012.754465.
[64] J. Hu, J. Zhang, L. Li, X. Bao, W. Deng, K. Chen, Chitosan-coated organosilica nanoparticles as a dual responsive delivery system of natural fragrance for axillary odor problem, Carbohydr. Polym. 269 (2021) 118277, https://doi.org/10.1016/j.carbpol.2021.118277.